https://doi.org/10.1016/j.est.2023.107427

A comprehensive modelling study of all vanadium redox flow battery: revealing the combined effects of electrode structure and surface property

Qijiao He [a, 1] , Zheng Li [a, 1], Idris Temitope Bello [a], Qidong Xu [a], Lingchao Xia [a], Chen Wang [a], Siyuan Zhao [a], Tianshou Zhao [b,*], Meng Ni [a,*]

[a] Department of Building and Real Estate, Research Institute for Sustainable Urban Development (RISUD) & Research Institute for Smart Energy (RISE), The Hong Kong Polytechnic University, Hung Hom, Kowloon, Hong Kong, China
[b] Department of Mechanical and Energy Engineering, Southern University of Science and Technology, Shenzhen 518055, China
[1] Qijiao HE and Zheng LI equally contributed to this work.
[*] Corresponding authors: zhaots@sustech.edu.cn (Tianshou Zhao); meng.ni@polyu.edu.hk (Meng Ni)

Abstract

To investigate the combined effects of electrode structural parameters and surface properties on the vanadium redox flow battery (VRFB) performance, a comprehensive model of VRFB is developed in this study. One feature of this study is that a practical range of working temperature is fully considered in the numerical simulations. Excellent VRFB performance was achieved by modified fibrous electrodes with 0.5 mm thickness and 0.9 porosity. The electrode with modified fibre of large diameter 20 μm shows improved battery performance with a low pressure drop. Without fibre modification, although VRFB with θ=7° aligned fibre electrode reaches the highest limiting current density, it has an evidently high pressure drop. At 323.15 K, the VRFB with θ=45° aligned fibre electrode showed 21% higher limiting current density and 36% lower pressure drop than VRFB with xy-plane isotropic electrode. Noteworthy, after the fibre surface modification, the sufficient specific surface area can be ensured, which leads to the insignificant effects of aligned electrode design. This model provides an insightful understanding of combined effects of electrode structure and surface property on the VRFBs performance at various temperatures.

Keywords

Vanadium redox flow battery; Numerical modelling; Temperature effects; Optimization; Electrospinning aligned electrode.

1. Introduction

In recent years, although solar and wind energy were used worldwide, they also created a new problem, namely, how to store the large amount of green energy collected in a safe and stable way [1-4]. Among many energy storage technologies, VRFB well meets the requirements with its long-life cycles, safe and stable operation, and flexibility [5]. The working principle of VRFB is shown in Fig.1. However, currently the performance of VRFB is strongly constrained by various voltage losses. Furthermore, as shown in Fig.1, in the VRFB system, pumps must be applied for pumping the electrolyte liquid. Therefore, the energy consumed by the pump considerably limits the overall energy efficiency of the VRFB system [6].

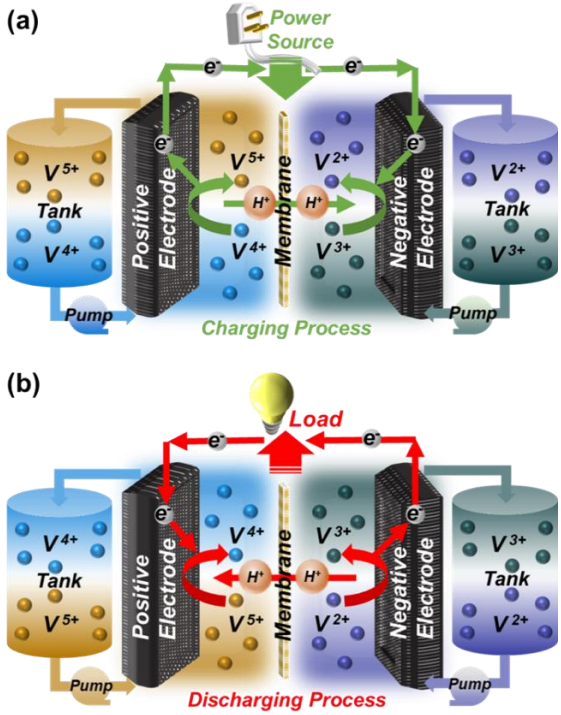

Fig.1 All vanadium flow battery working principle during charging process (a) and discharging process (b).

To enhance the VRFB performance and reduce the pump consumption, the structural parameters and surface properties of electrode should be optimized. On the one hand, by adjusting the structural parameters of electrode, the mass transfer in the porous media can be enhanced, subsequently reducing the concentration overpotential and pump loss. On the other hand, surface properties of electrode should be well-controlled, since they determine the amount of electrochemical active sites, which are crucial to the performance of the battery. Some experimental studies developed a variety of methods to control the electrode structural parameters and surface properties [7]. Kim et al. [8] prepared a new type of electrode with activity gradient carbon felt through a thermal oxidation procedure. Such a method efficiently

changes the surface properties of electrode, leading to a well-distributed electrochemical active region. It improves the VRFB discharge capacity and coulombic efficiency compared with pristine electrode. Hu et al. [9] reported a VRFB electrode with gradient bi-functional oxygen-containing groups, consisting of graphene oxide, reduced graphene oxide and graphene foam. Through different combinations of different composition materials to control the electrode properties, the electrode performance is remarkably enhanced, showing a high electrical conductivity and a high electrochemical catalytic activity. Their VFRB with this new electrode shows a high discharge capacity and high energy efficiency. Through a simple one-step etching method, Wang et al. [10] proposed a gradient-pore-oriented graphite felt electrode containing pores from nano- to micro-scale. Their electrode enhances the mass transfer within and forms enough active sites for electrochemical reactions. The VRFB assembled with the treated electrode exhibits 20% higher energy efficiency than the VRFB with untreated electrode at 200 mA cm^{-2}. In addition to using different method to fabricate gradient electrodes, using electrospinning to adjust electrode fibres properties is also an efficient approach to modify the electrode structure. Zhang et al. [11] fabricated aligned carbon nanofiber webs as electrode by electrospinning. The VRFB with the aligned electrode achieves an extremely high voltage efficiency of 87% at 60 mA cm^{-2}. The effects of the orientation of aligned fibres in electrode were studied by Sun et al. [12]. They applied aligned electrode in three different orientations for the VRFB with serpentine flow field. It is found that when the direction of aligned fibres is perpendicular to the direction of flow channels in serpentine flow field, the VRFB shows the highest limiting current density and largest discharge capacity. The model developed by Wan et al. [13] also demonstrated the promising future of aligned arrangement fibres in the VRFB's electrodes. The conversion of spent coffee beans into reduced graphene oxide [14] and tea waste into highly microporous electrode [15] were developed and tested respectively by Abbas et al. Both renewable biomass wastes have great potential to be applied as electrodes in VRFB due to their improved charge transfer, high electrocatalytic activity and excessive active sites.

Although some experimental studies have been done on modifying electrode structure and surface properties, they can only obtain the overall impacts of modified electrode on the VRFB's performance. The effects of individual electrode structural parameters or surface properties on VRFB performance are difficult to quantify through experimental studies. Although some numerical studies investigated the effects of individual electrode structural parameters such as electrode porosity, they could not offer a detailed and comprehensive understanding of the complex interaction between the electrode structural parameters and surface properties. Furthermore, the combined effects of electrode structural parameters and

surface properties on the various overpotentials and pump loss have not been fully studied yet. To fill these gaps, a 3D model is developed to gain a fundamental understanding on the effects of electrode structural parameters and surface properties. The complicated interrelationships between electrode structural parameters and surface properties are fully described numerically. More importantly, a noteworthy contribution of this work is the consideration of a more practical temperature range for VRFB operation, which has not been considered in the previous studies. Therefore, the predictions obtained in this work can be more accurate and general. The model developed in this work sheds lights on the interactions between the electrode structural parameters and surface properties and can be applied as a powerful tool for further electrode optimization and fabrication.

2. Mathematical model

A 3D model is built for a VRFB with interdigitated flow field shown in Fig.2. Flow field is applied in VRFB to decrease the ohmic loss, save the pump power and improve the uniformity of the reactants distribution in the electrolyte. The whole battery has a 20 mm × 20 mm active area with 5 branch inflow/outflow channels on each side, as shown in Fig.2 (a). The channel width is 1 mm. In the interdigitated flow field cases, since the mass transfer process between adjacent channel is similar, the unit computational domain can be applied, as shown in Fig.2 (b). The unit battery has a 16 mm × 2 mm active area and a half inflow/outflow channels which are symmetrical along the centre line on each side. The reactions occurring in electrodes of VRFB can be expressed as:

At positive electrode: $VO^{2+} + H_2O - e^- \underset{Discharge}{\overset{Charge}{\rightleftharpoons}} VO_2^+ + 2H^+$

At negative electrode: $V^{3+} + e^- \underset{Discharge}{\overset{Charge}{\rightleftharpoons}} V^{2+}$

The initial concentration settings in simulation refers to the process of configuring the electrolyte in the experiment [16]. First, 0.75 mol V_2O_5 solid powder is added to 1 L of 3.875 mol H_2SO_4 with following reaction

$2H^+ + V_2O_5 \leftrightarrow 2VO_2^+ + H_2O$

The concentration of H_2SO_4 solution is 3.875 mol L^{-1} (M) at the beginning. After dissolution and reaction, with the assumption that the sulfuric acid is fully dissociated, the solution consists of 1.5 M VO_2^+, 6.25 M H^+ and 3.875 M SO_4^{2-}. Then, in the pre-step, the following electrochemical reactions take place:

Oxidation reaction: $H_2O \leftrightarrow 0.5O_2 + 2H^+ + 2e^-$

Reduction reaction: $2VO_2^+ + 3e^- + 6H^+ \leftrightarrow VO^{2+} + V^{3+} + 3H_2O$

After the pre-step, the solution in the reduction side can be used as the initial electrolyte [17]. The initial electrolyte comprises 0.75 M VO^{2+}, 0.75 M V^{3+}, 4 M H^+ and 3.875 M SO_4^{2-}, which means the initial total vanadium ion concentration, $c_{V_{total}}^0$, is 1.5 M. After pre-charge reaction, 1) the electrolyte state of charge (SOC) is 0; 2) the positive electrolyte consists of 1.5 M VO^{2+}, 4.75 M H^+ and 3.875 M SO_4^{2-}; 3) the negative electrolyte consists of 1.5 M V^{3+}, 3.25 M H^+ and 3.875 M SO_4^{2-}. After charge reaction, 1) SOC is 1; 2) the positive electrolyte consists of 1.5 M VO_2^+, 6.25 M H^+ and 3.875 M SO_4^{2-}; 3) the negative electrolyte consists of 1.5 M V^{2+}, 4.75 M H^+ and 3.875 M SO_4^{2-}. The inlet species concentration, c_i^{in}, is determined by the SOC_{in} except SO_4^{2-} as constant:

$$c_{VO_2^+}^{in} = c_{V^{2+}}^{in} = SOC_{in} \cdot c_{V_{total}}^0$$

$$c_{VO^{2+}}^{in} = c_{V^{3+}}^{in} = (1 - SOC_{in}) \cdot c_{V_{total}}^0$$

$$c_{H^+_{pos}}^{in} = 4M + (SOC_{in} + 0.5) \cdot c_{V_{total}}^0$$

$$c_{H^+_{neg}}^{in} = 4M + (SOC_{in} - 0.5) \cdot c_{V_{total}}^0$$

$$c_{SO_4^{2-}{}_{pos}}^{in} = c_{SO_4^{2-}{}_{neg}}^{in} = \left(1\ M + 2.5 \times c_{V_{total}}^0\right)/2$$

2.1 Model assumptions

The assumptions and simplifications used in the present work are listed as follows:

1. The VRFB is in steady state operation, considering that the two reservoirs are sufficiently large.
2. The entire computational domain is assumed to be isothermal.
3. The fluid flow is incompressible.
4. The membrane is set as an ionic conductor with no mass transport or ion diffusion, except for proton transport which is considered as flux at both membrane surfaces.
5. The possible side reactions such as oxygen and hydrogen evolutions are neglected.

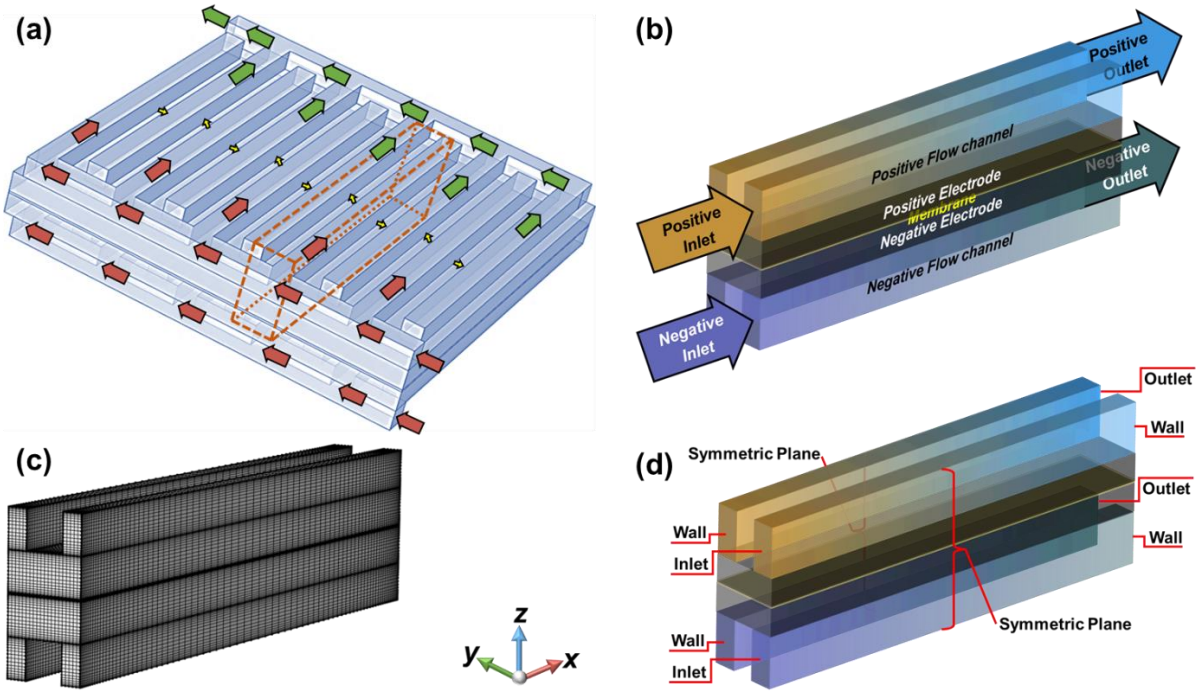

Fig.2 Schematic diagram of the whole battery computational domain (a), the unit computational domain of the interdigitated flow field VRFB (b), the computational mesh (c) and the boundary condition setting (d).

2.2 Fluid flow and mass transport model

The mass and the momentum conservation for electrolyte in both the channel and porous electrode can be expressed with the continuity equation, Navier-Stokes equation, and Brinkman equation respectively:

$$\rho \nabla \cdot \vec{u} = 0 \tag{1}$$

$$\rho(\vec{u} \cdot \nabla)\vec{u} = -\nabla p + \nabla \cdot [\mu(\nabla \vec{u} + (\nabla \vec{u})^T)] \tag{2}$$

$$\frac{\rho}{\varepsilon^2}(\vec{u} \cdot \nabla)\vec{u} = -\nabla p + \nabla \cdot \left[\frac{\mu}{\varepsilon}(\nabla \vec{u} + (\nabla \vec{u})^T)\right] - \frac{\mu}{\kappa}\vec{u} \tag{3}$$

where ρ is fluid density (mol m^{-3}), u is the velocity (m s^{-1}), p is the pressure (Pa), μ is the dynamic viscosity of the fluid (Pa s), ε is the porosity of the porous electrode, which is defined as the ratio of the volume of the pores to the total volume of the electrode material, and κ is the permeability of the porous electrode. According to fitting formula of experimental data, the two temperature-dependent parameters, electrolyte density [18] and dynamic viscosity [19], are respectively set as follows:

$$\rho_{pos} = 1.3447\ g \cdot ml^{-1} - 0.0006\ g \cdot (ml \cdot K)^{-1} \times \left(T - T_{ref}\right) \tag{4}$$

$$\rho_{neg} = 1.3686\ g \cdot ml^{-1} - 0.0006\ g \cdot (ml \cdot K)^{-1} \times \left(T - T_{ref}\right) \tag{5}$$

$$\mu_{pos} = \rho_{pos} \cdot \upsilon_{pos} = \rho_{pos} \times 4.5 \times \exp(-0.06 \times (T - T_0) + 1.6) \tag{6}$$

$$\mu_{neg} = \rho_{neg} \cdot \upsilon_{neg} = \rho_{neg} \times 8 \times \exp(-0.055 \times (T - T_0) + 1.4) \times (1 - SOC) + \rho_{pos} \cdot \upsilon_{pos} \cdot SOC \tag{7}$$

where υ is the kinetic viscosity of the fluid ($m^2\ s^{-1}$), T is the temperature of fluid (K), $T_{ref} =$ 298.15 K and $T_0 = 273.15$ K. The specific surface area of the electrode, a, was determined by fibre diameter and porosity, which can be calculated by [20]:

$$a = \frac{4(1-\varepsilon)}{d_f} \tag{8}$$

where d_f is the fiber diameter (m). The permeability of the porous electrode is expressed as [21]:

$$\kappa = \frac{d_f^2 \varepsilon^3}{16 k_{ck}(1-\varepsilon)^2} \tag{9}$$

where k_{ck} is the dimensionless Carman-Kozeny constant which depends on the shape and orientation of the fibrous material. According to Ref. [22], for a flow parallel to the cylinder, the Carman-Kozeny constant is expressed as:

$$k_{ck,\parallel} = \frac{2\varepsilon^3}{(1-\varepsilon)\left[2\ln\frac{1}{1-\varepsilon} - 3 + 4(1-\varepsilon) - (1-\varepsilon)^2\right]} \tag{10}$$

For a flow perpendicular to the cylinder, the Carman-Kozeny constant is found to be:

$$k_{ck,\perp} = \frac{\frac{2\varepsilon^3}{(1-\varepsilon)}}{\ln\frac{1}{(1-\varepsilon)} - \frac{1-(1-\varepsilon)^2}{1+(1-\varepsilon)^2}} \tag{11}$$

For previous electrode calculations, we generally treated them as isotropic electrodes, so the k_{ck} is set to be 4.28 [23]. For the aligned electrode studies in this paper, the porosity of electrode is set to 0.9. Thus the $k_{ck,\parallel}$ and $k_{ck,\perp}$ can be calculated as 0.73 and 11.03, respectively. Further, we can obtain the permeability tensor of different fibre orientations to the flow field [24]:

$$[k] = \begin{bmatrix} k_{xx} & k_{xy} & \\ k_{yx} & k_{yy} & \\ & & k_{zz} \end{bmatrix} =$$

$$\begin{bmatrix} k_\parallel \cos^2\theta + k_\perp \sin^2\theta & k_\parallel \cos\theta \sin\theta - k_\perp \cos\theta \sin\theta & \\ k_\parallel \cos\theta \sin\theta - k_\perp \cos\theta \sin\theta & k_\parallel \sin^2\theta + k_\perp \cos^2\theta & \\ & & k_\perp \end{bmatrix} \tag{12}$$

where θ is the angle of fibre to the x-axis as shown in Fig.3. Since the arrangement of aligned electrode only varies on the xy-plane, the flow along the z-axis is always perpendicular to the fibre.

For isotropic arrangement in xy-plane, $[k] = k\begin{bmatrix} 1 & 0 \\ 0 & 1 \end{bmatrix}$, then the permeability tensor can be calculated as $\begin{bmatrix} 1.065 \times 10^{-10} & 0 & 0 \\ 0 & 1.065 \times 10^{-10} & 0 \\ 0 & 0 & 4.13 \times 10^{-11} \end{bmatrix}$.

The calculated result shows that the electrode has two same in-plane permeability, which is higher than the through-plane permeability. This result is consistent with the literature data [25].

For parallel orientation arrangement, the permeability tensor is

$$\begin{bmatrix} 6.24\times10^{-10} & 0 & 0 \\ 0 & 4.13\times10^{-11} & 0 \\ 0 & 0 & 4.13\times10^{-11} \end{bmatrix}.$$

For vertical orientation arrangement, the permeability tensor is

$$\begin{bmatrix} 4.13\times10^{-11} & 0 & 0 \\ 0 & 6.24\times10^{-10} & 0 \\ 0 & 0 & 4.13\times10^{-11} \end{bmatrix}.$$

For $\theta = 45°$ arrangement, the permeability tensor is

$$\begin{bmatrix} 3.33\times10^{-10} & 2.91\times10^{-10} & 0 \\ 2.91\times10^{-10} & 3.33\times10^{-10} & 0 \\ 0 & 0 & 4.13\times10^{-11} \end{bmatrix}.$$

For $\theta = 7°$ arrangement, the permeability tensor is

$$\begin{bmatrix} 6.15\times10^{-10} & 7.05\times10^{-11} & 0 \\ 7.05\times10^{-11} & 5\times10^{-11} & 0 \\ 0 & 0 & 4.13\times10^{-11} \end{bmatrix}.$$

The schematic of the above setup can be found in Fig.3.

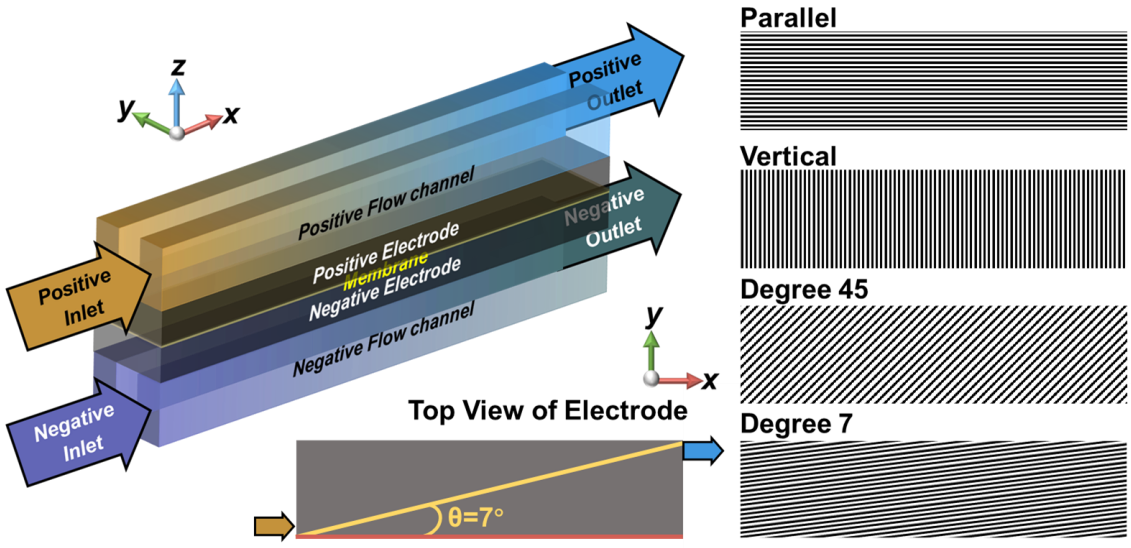

Fig.3 Schematic diagrams of the different aligned electrode configurations.

Nernst-Plank equation [26] is employed to describe the transport of dilute species in the porous electrode which comprises diffusive, migrative, and convective items:

$$\vec{N}_i = -D_i^{eff}\nabla c_i - \frac{z_i c_i D_i^{eff}}{RT} F\nabla\phi_l + \vec{u}c_i \tag{13}$$

$$\nabla\cdot\vec{N}_i = S_i \tag{14}$$

where the index i represents the species, and $\vec{N}_i$ is the flux of the species (mol m^{-2} s^{-1}). S_i is the species molar source term, which represents the generation rate of species due to the electrochemical reactions. c_i and z_i are molar concentration (mol m^{-3}) and charge number of species i, respectively. F is Faraday's constant (= 96485 C mol^{-1}). ϕ_l is the potential in the electrolyte (V).

The effective diffusivity (m^2 s^{-1}) D_i^{eff} is corrected according to the Bruggeman correction [27]:

$$D_i^{eff} = \varepsilon^{1.5} D_i \tag{15}$$

The empirical equation is used based on the linearity of the diffusion coefficients of 1.5 M electrolytes with the temperature and the SOC of vanadium ions [19]:

$$\ln D_{VO^{2+},VO_2^+} = -1.04 \times (1 + 1.27 \times SOC - 5.87 \times SOC^2) - 4122.59 \times \left(\frac{1}{T}\right) \tag{16}$$

$$\ln D_{V^{2+},V^{3+}} = -5.67 \times (1 - 0.14 \times SOC - 0.61 \times SOC^2) - 2713.09 \times \left(\frac{1}{T}\right) \tag{17}$$

2.3 Electrochemical reaction model

Electricity produced from electrochemical oxidation and reduction reactions can be described by the electrochemical reaction model. The general Butler-Volmer equation is used to link the current density with activation overpotential. Vanadium ions in different valence states participate in electrochemical reactions as redox couples.

Charge transport in the electrode for positive side is solved as:

$$\nabla \cdot \vec{i}_s = -\sigma_s^{eff} \nabla^2 \phi_s = i_{pos} \tag{18}$$

$$\nabla \cdot \vec{i}_l = -\sigma_l^{eff} \nabla^2 \phi_l = -i_{pos} \tag{19}$$

where $\vec{i}_s$is the current density in the electrode (A m^{-2}), $\vec{i}_l$ is the current density in the electrolyte. σ_s^{eff} and σ_l^{eff} represent the effective electronic and ionic conductivity (S m^{-1}) derived from the following expressions. ϕ_s and ϕ_l are the electronic potential and ionic potential.

The membrane is set only conductive through proton transport as an electric insulator. The ionic current density at the membrane, i_{mem}, determines the magnitude of the proton flux on membrane surfaces. For positive membrane surface, the proton flux is $-i_{mem}/F$. For negative membrane surface, the proton flux is i_{mem}/F. The membrane is modeled by using Ohm's law. The σ_m is the membrane conductivity.

$$\nabla \cdot \vec{i}_l = -\sigma_m \nabla^2 \phi_l = -i_{mem} \tag{20}$$

Similar equations for charge transport are applied to the negative electrode. The ionic conductivity σ_l is calculated from the empirical equation [28].

$$\nabla \cdot \vec{i}_s = -\sigma_s^{eff} \nabla^2 \phi_s = i_{neg} \tag{21}$$

$$\nabla \cdot \vec{i}_l = -\sigma_l^{eff} \nabla^2 \phi_l = -i_{neg} \quad (22)$$

$$\sigma_s^{eff} = (1-\varepsilon)^{1.5} \sigma_s \quad (23)$$

$$\sigma_l^{eff} = \varepsilon^{1.5} \sigma_l \quad (24)$$

$$\sigma_{l,pos} = (1.8 \times (T - T_0) + 93.503) \times SOC + (4.6713 \times (T - T_0) + 172.07) \quad (25)$$

$$\sigma_{l,neg} = (0.705 \times (T - T_0) + 55.042) \times SOC + (2.6176 \times (T - T_0) + 122.37) \quad (26)$$

where $T_0 = 273.15$ K. The unit of conductivity calculated from Eq. (25) and (26) is mS cm^{-1}. The source term S_i of different species i is related to the electrochemical reaction rate i_{pos} and i_{neg}. For the positive electrode: $S_{VO^{2+}} = i_{pos}/F$, $S_{VO_2^+} = -i_{pos}/F$, $S_{H^+} = -2i_{pos}/F$. For the negative electrode: $S_{V^{2+}} = i_{neg}/F$, $S_{V^{3+}} = -i_{neg}/F$. The local current density, which is also termed as transfer current density, i_{loc}, is defined as, i_{pos}/a in positive electrode and i_{neg}/a in negative electrode. The electrochemical reactions occurring on the surfaces of solid fiber in the electrode can be expressed by the Butler-Volmer equation [29]:

$$i_{pos} = aFk_{pos}^0 c_{VO^{2+}}^{\alpha_{c,pos}} c_{VO_2^+}^{\alpha_{a,pos}} \left[\frac{c_{VO_2^+}^s}{c_{VO_2^+}} \exp\left(-\frac{\alpha_{c,pos} F \eta_{pos}}{RT}\right) - \frac{c_{VO^{2+}}^s}{c_{VO^{2+}}} \exp\left(\frac{\alpha_{a,pos} F \eta_{pos}}{RT}\right) \right] \quad (27)$$

$$i_{neg} = aFk_{neg}^0 c_{V^{2+}}^{\alpha_{c,neg}} c_{V^{3+}}^{\alpha_{a,neg}} \left[\frac{c_{V^{3+}}^s}{c_{V^{3+}}} \exp\left(-\frac{\alpha_{c,neg} F \eta_{neg}}{RT}\right) - \frac{c_{V^{2+}}^s}{c_{V^{2+}}} \exp\left(\frac{\alpha_{a,neg} F \eta_{neg}}{RT}\right) \right] \quad (28)$$

where k_{pos}^0 and k_{neg}^0 is the reaction rate constant of the reactions occurring in positive and negative sides, respectively. $\alpha_{a,pos}$ and $\alpha_{c,pos}$ are anodic and cathodic charge transfer coefficient of positive half-reaction, $\alpha_{a,neg}$ and $\alpha_{c,neg}$ are anodic and cathodic charge transfer coefficient of negative half-reaction. c_i^s is the concentration at the fiber surface of species i. R is the ideal gas constant. Overpotentials η_{pos} and η_{neg} are defined as follows:

$$\eta_{pos} = \phi_{s,pos} - \phi_{e,pos} - E_{eq,pos} \quad (29)$$

$$\eta_{neg} = \phi_{s,neg} - \phi_{e,neg} - E_{eq,neg} \quad (30)$$

Equilibrium potentials are calculated via:

$$E_{eq,pos} = E_{pos}^0 + \frac{RT}{F} \ln\left(\frac{c_{VO_2^+} c_{H^+}^2}{c_{VO^{2+}}}\right) \quad (31)$$

$$E_{eq,neg} = E_{neg}^0 + \frac{RT}{F} \ln\left(\frac{c_{V^{3+}}}{c_{V^{2+}}}\right) \quad (32)$$

The standard potentials E_{neg}^0 and E_{pos}^0 are related to the temperature [30].

$$E_{pos}^0 = E_{pos,ref}^0 + \left.\frac{dE_0}{dT}\right|_{pos} (T - T_{ref}) = -0.255 + \frac{\Delta S_{pos}}{nF}(T - T_{ref}) \quad (33)$$

$$E_{neg}^0 = E_{neg,ref}^0 + \left.\frac{dE_0}{dT}\right|_{neg} (T - T_{ref}) = 1.004 + \frac{\Delta S_{neg}}{nF}(T - T_{ref}) \quad (34)$$

where the $E^0_{pos,ref}$ and $E^0_{neg,ref}$ are the standard equilibrium potentials at T_{ref} = 298.15 K. The temperature dependent term for the negative or positive electrode is related to the entropy changes ΔS_{neg}= 21.7 J mol^{-1} K^{-1} and ΔS_{pos}== 100 J mol^{-1} K^{-1} during the electrochemical reactions [31]. n denotes the number of charge transferred in the electrochemical reaction, which value is 1 in the calculation.

A quasi-equilibrium state assumption is adopted for the ions transport considering that SOC of electrolyte changes slowly due to relatively small volume of electrolyte in the cell compared with that in the reservoirs. The vanadium ions concentration at the surface of carbon fibers can be calculated by balancing the reaction rate and the rate of ion transfer from the bulk to the interface. Therefore, the local flux at the surface of the positive electrode is [29]:

$$N^s_{VO^{2+}} = k_m\left(c_{VO^{2+}} - c^s_{VO^{2+}}\right) = -i_{pos}/(aF)$$

$$= k^0_{pos} c^{\alpha_{c,pos}}_{VO^{2+}} c^{\alpha_{a,pos}}_{VO_2^+} \left[\frac{c^s_{VO^{2+}}}{c_{VO^{2+}}} \exp\left(\frac{\alpha_{a,pos} F\eta_{pos}}{RT}\right) - \frac{c^s_{VO_2^+}}{c_{VO_2^+}} \exp\left(-\frac{\alpha_{c,pos} F\eta_{pos}}{RT}\right)\right] \quad (35)$$

$$N^s_{VO_2^+} = k_m\left(c_{VO_2^+} - c^s_{VO_2^+}\right) = i_{pos}/(aF)$$

$$= k^0_{pos} c^{\alpha_{c,pos}}_{VO^{2+}} c^{\alpha_{a,pos}}_{VO_2^+} \left[\frac{c^s_{VO_2^+}}{c_{VO_2^+}} \exp\left(-\frac{\alpha_{c,pos} F\eta_{pos}}{RT}\right) - \frac{c^s_{VO^{2+}}}{c_{VO^{2+}}} \exp\left(\frac{\alpha_{a,pos} F\eta_{pos}}{RT}\right)\right] \quad (36)$$

Combining Eqs. (35) and (36), the concentrations of VO^{2+} and VO_2^+ at the carbon fiber surface are derived as

$$c^s_{VO^{2+}} = \frac{B_1 c_{VO_2^+} + (1+B_1) c_{VO^{2+}}}{1 + A_1 + B_1} \quad (37)$$

$$c^s_{VO_2^+} = \frac{A_1 c_{VO^{2+}} + (1+A_1) c_{VO_2^+}}{1 + A_1 + B_1} \quad (38)$$

where

$$A_1 = \frac{k^0_{pos}}{k_m} c^{\alpha_{c,pos}-1}_{VO^{2+}} c^{\alpha_{a,pos}}_{VO_2^+} \exp\left(\frac{\alpha_{a,pos} F\eta_{pos}}{RT}\right) \quad (39)$$

$$B_1 = \frac{k^0_{pos}}{k_m} c^{\alpha_{c,pos}}_{VO^{2+}} c^{\alpha_{a,pos}-1}_{VO_2^+} \exp\left(\frac{-\alpha_{c,pos} F\eta_{pos}}{RT}\right) \quad (40)$$

The local flux at the surface of the negative electrode is:

$$N^s_{V^{2+}} = k_m\left(c_{V^{2+}} - c^s_{V^{2+}}\right) = -i_{neg}/(aF)$$

$$= k^0_{neg} c^{\alpha_{c,neg}}_{V^{2+}} c^{\alpha_{a,neg}}_{V^{3+}} \left[\frac{c^s_{V^{2+}}}{c_{V^{2+}}} \exp\left(\frac{\alpha_{a,neg} F\eta_{neg}}{RT}\right) - \frac{c^s_{V^{3+}}}{c_{V^{3+}}} \exp\left(-\frac{\alpha_{c,neg} F\eta_{neg}}{RT}\right)\right] \quad (41)$$

$$N^s_{V^{3+}} = k_m\left(c_{V^{3+}} - c^s_{V^{3+}}\right) = i_{neg}/(aF)$$

$$= k^0_{neg} c^{\alpha_{c,neg}}_{V^{2+}} c^{\alpha_{a,neg}}_{V^{3+}} \left[\frac{c^s_{V^{3+}}}{c_{V^{3+}}} \exp\left(-\frac{\alpha_{c,neg} F\eta_{neg}}{RT}\right) - \frac{c^s_{V^{2+}}}{c_{V^{2+}}} \exp\left(\frac{\alpha_{a,neg} F\eta_{neg}}{RT}\right)\right] \quad (42)$$

Combining Eqs. (41) and (42), the concentrations of V^{2+} and V^{3+} at the carbon fiber surface are derived as

$$c_{V^{2+}}^{S} = \frac{B_2 c_{V^{3+}} + (1+B_2) c_{V^{2+}}}{1 + A_2 + B_2} \tag{43}$$

$$c_{V^{3+}}^{S} = \frac{A_2 c_{V^{2+}} + (1+A_2) c_{V^{3+}}}{1 + A_2 + B_2} \tag{44}$$

where

$$A_2 = \frac{k_{neg}^0}{k_m} c_{V^{2+}}^{\alpha_{c,neg}-1} c_{V^{3+}}^{\alpha_{a,neg}} \exp\left(\frac{\alpha_{a,neg} F \eta_{neg}}{RT}\right) \tag{45}$$

$$B_2 = \frac{k_{neg}^0}{k_m} c_{V^{2+}}^{\alpha_{c,neg}} c_{V^{3+}}^{\alpha_{a,neg}-1} \exp\left(\frac{-\alpha_{c,neg} F \eta_{neg}}{RT}\right) \tag{46}$$

Based on Arrhenius law, the reaction rate constants, k_{pos}^0 and k_{neg}^0 are temperature dependent and can be written as follows:

$$k_{pos}^0 = k_{pos,ref}^0 \exp\left(-\frac{\Delta G_{pos}^0}{R}\left(\frac{1}{T_{ref}} - \frac{1}{T}\right)\right) = k_{pos,ref}^0 \exp\left(\frac{nFE_{pos}^0}{R}\left(\frac{1}{T_{ref}} - \frac{1}{T}\right)\right) \tag{47}$$

$$k_{neg}^0 = k_{neg,ref}^0 \exp\left(-\frac{\Delta G_{neg}^0}{R}\left(\frac{1}{T_{ref}} - \frac{1}{T}\right)\right) = k_{neg,ref}^0 \exp\left(\frac{nFE_{neg}^0}{R}\left(\frac{1}{T_{ref}} - \frac{1}{T}\right)\right) \tag{48}$$

where $\Delta G_{pos}^0 = -nFE_{pos}^0$ and $\Delta G_{neg}^0 = -nFE_{neg}^0$ are the standard Gibbs free energy change for the respective reaction. $k_{pos,ref}^0$ and $k_{neg,ref}^0$ are the standard reaction rate constants at $T_{ref} = 298.15$ K. The mass trasfer cefficient can be sloved by the measured limiting currents [20,32]. Thus, the local mass transfer coefficient can be calculated approximately [33,34]:

$$k_m = 8.85 \times 10^{-4} |\vec{u}|^{0.9} \tag{49}$$

The parameters of electrochemical reactions, material properties, geometry, and operating conditions are listed in Table 1 and Table 2. Although a slight increase in the electron transfer coefficient at room temperature to higher temperature has been reported in the literature [35], it has been verified that the constants used in most of the literature [29] is feasible with acceptable accuracy.

Table 1 Electrochemical parameters and material properties.

Symbols	Parameters (Unit)	Value
$\alpha_{a,pos}$	Anodic charge transfer coefficient for the positive side	0.5 [29,35,36]
$\alpha_{c,pos}$	Cathodic charge transfer coefficient for the positive side	0.5 [29,35,36]
$\alpha_{a,neg}$	Anodic charge transfer coefficient for the negative side	0.5 [29,35,36]
$\alpha_{c,neg}$	Cathodic charge transfer coefficient for the negative side	0.5 [29,35,36]
σ_s	Electrode conductivity (S m^{-1})	5000 [37]
σ_m	Membrane conductivity (S m^{-1})	12 [38]

$k^0_{pos,ref}$	The standard reaction rate constant of the negative side (m s^{-1})	6.8×10^{-7} [39]
$k^0_{neg,ref}$	The standard reaction rate constant of the negative side (m s^{-1})	1.7×10^{-7} [40]
$E^0_{pos,ref}$	Standard equilibrium potentials of positive side at 298.15 K (V)	1.004 [41]
$E^0_{neg,ref}$	Standard equilibrium potentials of negative side at 298.15 K (V)	-0.255 [41]
D_{H^+}	Proton diffusion coefficient (m^2 s^{-1})	9.3×10^{-9} [42]
$D_{SO_4^{2-}}$	SO_4^{2-} diffusion coefficient (m^2 s^{-1})	1.1×10^{-9} [42]

Table 2 Operating and geometric parameters.

Symbols	Parameters (Unit)	Value
T	Operating temperature (K)	273.15 ~ 323.15
V_{work}	Working voltage (V)	Open-circuit voltage (OCV) ~ 0.15
ε	Electrode porosity	0.8 ~ 0.93
a	Specific surface area (m^{-1})	Original ~ 5×10^5
d_f	Carbon electrode fiber (μm)	5 ~ 20
Q_{in}	Inlet flow rate (ml min^{-1})	10 ~ 30
$thick_e$	Electrode thickness (mm)	0.5 ~ 1.5
$thick_m$	Membrane thickness (μm)	50
SOC_{in}	SOC of inlet	0.5
$channel_l$	Channel length (mm)	16
$channel_w$	Channel width (mm)	1
$channel_d$	Channel depth (mm)	1
$channel_n$	Inflow channel number	5

2.4 Boundary conditions and model solving

Fig.2 (d) shows the boundary conditions of the unit computational domain of the VRFB with interdigitated flow field. It is worth noting that the inflow velocity boundary of the unit calculational domain is set to be v_{in}, which can be converted by using following equation

$$v_{in} = \frac{Q_{in}}{channel_n \times 2 \times A_{in}} = \frac{Q_{in}}{channel_n \times 2 \times \frac{channel_w}{2} \times channel_d}$$

where A_{in} is the cross-sectional area of the half inflow channel in calculational domain. Since the calculated inflow channel domain is only half the actual size, the inflow rate Q_{in} also needs to be divided by two. The inlet species concentration, c_i^{in}, is given in details at the beginning of this section. At the outlet of the outflow channel, the pressure is set to be zero as the reference

and concentration gradient is assumed to be zero. Zero potential is adopted at the contact surface of the negative porous electrode and the current collector. Working voltage, V_{work}, is applied to the contact surface of the positive porous electrode and the current collector. The two ends of the unit in the zx-plane are set as symmetric plane in mass, species, and charge transfer. All the other boundaries are impermeable to the mass, species, and charge transfer.

2.5 Model validation and mesh independence

The above equations are solved based on the finite element method. The relative tolerance is set to 1×10^{-4}. Based on the experimental data [19], we validated the model at inlet flow rate 20 mL min^{-1}, current density 60 mA cm^{-2}, 1.5 M total vanadium ion concentration, 0.06 ~ 0.94 SOC, and ambient temperatures 273.15 K ~ 323.15 K through discharge curves. As depicted in Fig.4 (a), the simulation results show good agreement with experimental data [19]. Fig.4 (b) shows the mesh independence validation. The operating voltage, 0.5 V, is applied to VRFB for checking the dependence of the calculated current density on the number of degrees of freedom at different temperatures. It can be seen that with the increased number of degrees of freedom, the current density at 273.15 K gradually approaches at 613 mA cm^{-1}, while the current density at 293.15 K gradually stabilizes at 841 mA cm^{-1} and current density at 323.15 K gradually stabilizes at 1061 mA cm^{-1}. Considering the accuracy and computational cost, the number of 414,861 is adopted for the degrees of freedom in the subsequent simulations. The final selected computational mesh can be found in Fig.2 (c).

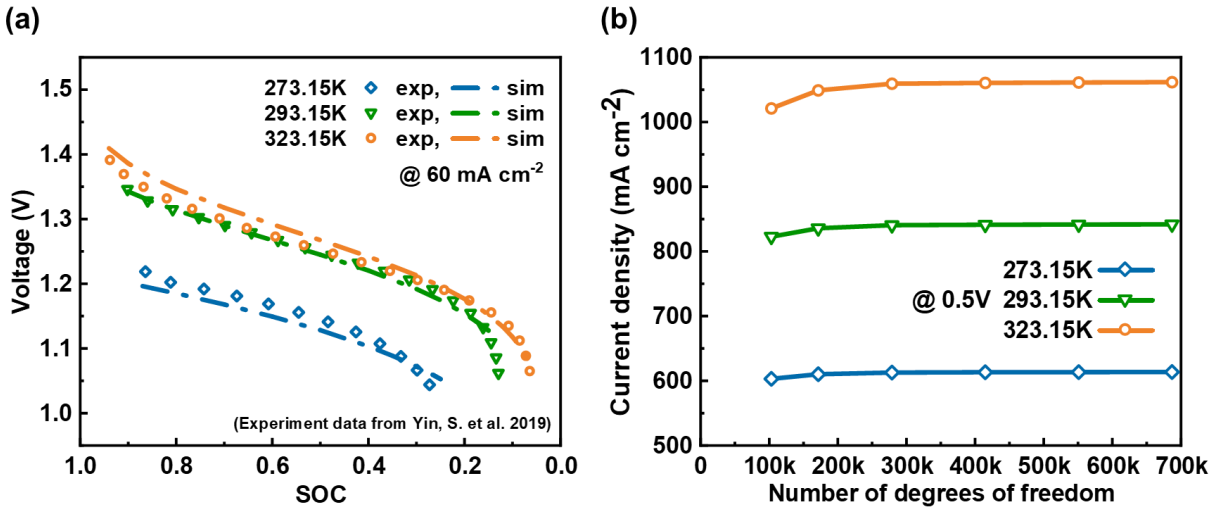

Fig.4 (a) Model validation for the VRFBs working at various temperature; (b) Mesh independence check.

3. Results and discussion

The main objective of the present work is to study and fully describe the complicated interrelationships of electrode structural parameters and surface properties. Another objective is the consideration of a more practical temperature range for VRFB operation, which has not been considered in the previous studies. Finally, the potential aligned electrodes are evaluated as a hopeful design. In the subsequent parametric studies, the polarization curves were calculated with 0.5 inlet SOC, same 1.5 M total ion concentration and same operating temperatures, compared to validation conditions. Other detailed operating conditions and electrode parameters are provided in each sub-section respectively.

3.1 Combined effects of electrode thickness and specific surface area

In this sub-section, the inlet flow rate is 30 ml min^{-1}, SOC of inlet is set as 0.5, the electrode porosity is 0.9 and the carbon electrode fibre diameter is set as 10 μm. The specific surface area of original electrode without modification is calculated from Eq. (8). Other detailed operating conditions and electrode parameters are labelled in each sub-figure respectively. The combined effects of the electrode thickness and the specific surface area at various temperatures on polarization curves are shown in Fig.5 (a-c).

At 273.15 K, the VRFB with a 0.5 mm thick original electrode performs worse than VRFB with a 1.5 mm thick original electrode when the voltage is higher than 0.9 V, due to the insufficient total reaction site in the thin electrode. In addition, with the decreased working temperature, the electrochemical activity decreases, also leading to a higher activation loss. To get sufficient reaction sites and reduce activation loss, the fibre specific surface area is modified as same value (2.5×10^5 m^2 m^{-3}). After the fibre surface modification, no obvious difference is observed in the performance of VRFB with different electrode thicknesses when the voltage is higher than 1.05 V at 273.15 K. At 293.15 K, the VRFB with a thin original electrode performs worse than VRFB with a thick original electrode when the voltage is higher than 1.0 V. The mentioned voltage range changes from 0.9 V~OCV at 273.15 K to 1.0 V~OCV at 293.15 K, because the increasing electrochemical activity leads to less activation loss difference. At 323.15 K, the effects of electrode thickness on battery performance are not obvious when the operating voltage is higher than 1.15 V with original fibre.

After the fibre surface modification, the VRFB with a thin electrode delivers a larger current density than VRFB with a thick electrode at the same working voltage at both 293.15 K and 323.15 K. The slope of battery polarization curve with a 1.5 mm thick electrode is steeper than that of battery with a 0.5 mm thick electrode at all temperatures with original and modified

electrode fibre. This is due to the larger ohmic loss caused by the thicker electrode, which decreases the voltage significantly. Moreover, since electrolyte ion conductivity increases with the increasing temperature, the slope of the polarization curve of VRFB at 273.15 K is sharper than VRFB at 323.15 K with the same electrode thickness, no matter using original or modified fibre. With the increasing current density, the VRFB with a 0.5 mm thick original electrode performs better until the voltage decreases to 0.4 V at 293.15 K or decreases to 0.7 V at 323.15 K. At different temperatures, the VRFB with an original thin electrode shows an evident concentration overpotential under high current density, especially at high temperatures. Limited by the insufficient surface area in a 0.5 mm thick electrode, the limiting current densities of the VRFBs at different temperatures are all around 950 mA cm^{-2}. After the fibre surface modification, the battery performance improves significantly, especially at high temperatures. Thin electrode can reduce the ohmic overpotential. When the electrode is thin, the ohmic impedance mainly comes from the electrolyte, and it is necessary to keep the electrolyte temperature not too low to reduce the ohmic impedance. Meanwhile, the influence of electrode thickness on battery performance is more obvious. For example, from Fig.5 (a-c), at working potential of 0.8 V, this more obvious difference is mainly due to the fact that the modified electrode has a larger specific surface area than the conventional electrode. Even if the local current density difference is small, the battery current density difference is more significant due to the effect of large specific surface area. At 273.15 K, 0.8 V, compared with VRFB with conventional electrode (0.5 mm), the performance of VRFB with a modified electrode (0.5 mm) increases by 133.79%. This enhancement in the performance decreases slightly to 133.18% at 323.15 K. The simulation results are consistent with the Ref. [15]. The modified electrode with highly microporous has sufficient active sites compared to the conventional electrode, which greatly improves the performance of the battery. Besides, the modified electrode can be prepared from renewable waste, which has a promising practical VRFB applications.

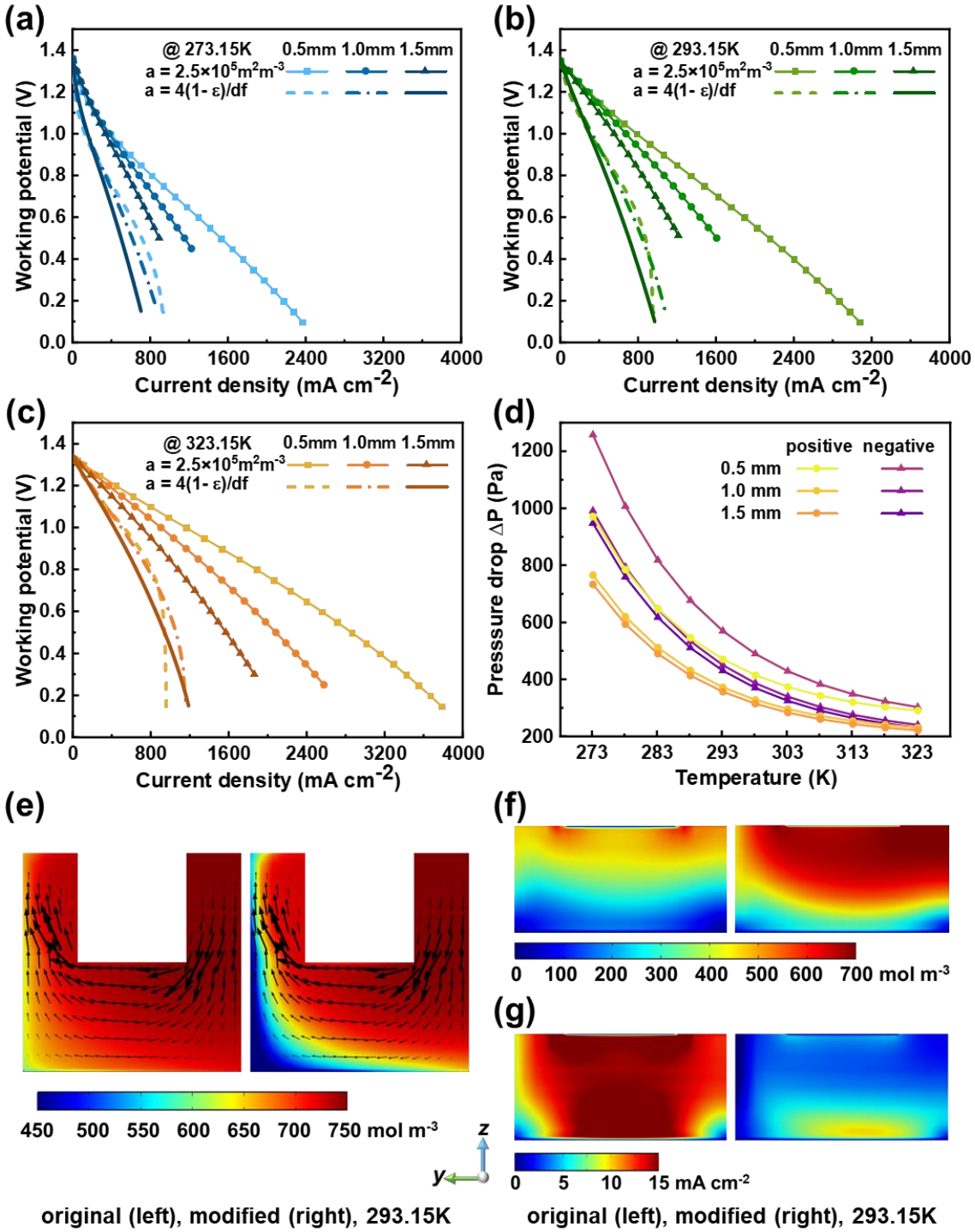

Fig.5 Polarization curves of VRFB with different electrode thickness and electrode modification at 273.15 K (a), 293.15 K (b) and 323.15 K (c); Pressure drop of VRFB with temperature effects (d); V^{5+} bulk concentration distribution with velocity component (scale-up factor 50) in yz-direction (e), V^{5+} surface concentration distribution (f), and local current density distribution (g) in yz-plane at middle of channel length (x=8 mm).

As shown in Fig.5 (d), due to the different viscosities of the positive and negative electrolyte, the pressure drop of the negative electrode is larger than that of the positive electrode, leading

to a higher pump energy consumption. The difference between them increases with the decreasing temperature. In addition, the VRFB with a 0.5 mm thick shows the highest pressure drop at different temperatures. When the electrode thickness increases to 1.0 mm, the pressure drop in the negative electrode decreases by 20%, while the pressure drop in the positive electrode decreases by 25%. However, when the thickness further increases to 1.5 mm, the decreases in the pressure drop of negative and positive electrodes are insignificant. Therefore, the electrochemical performance and the pump energy consumption can be balanced by controlling the electrode thickness at an optimal value. Due to a larger specific surface area in the modified electrode, the reactant conversion is higher as demonstrated in Fig.5 (e). Combining Fig.5 (f) with (g), under the same output, the local current density in the conventional electrode is larger than that in the modified electrode due to the insufficient specific surface area. This can lead to a lower surface reactant concentration in the conventional electrode.

3.2 Combined effects of electrode porosity and specific surface area

The SOC of inlet is set as 0.5 and the carbon electrode fibre diameter is set as 10 μm in this sub-section. The porosity of 0.8 ~ 0.93 is chosen for calculation because commercial electrodes generally have a porosity of 0.95. After installation, slight compression is needed for sealing and long-term stability, thus the porosity is lower than 0.93 according to different compression ratio. Further compression of the electrode makes the pump consumption rise rapidly and is possible to crush the membrane in the middle, thus 0.8 is selected as the lower porosity limit for the study. Other detailed operating conditions and electrode parameters are labelled in each sub-figure, respectively. The combined effects of electrode porosity and specific surface area at various temperatures on the VRFB performance at 0.8 V are shown in Fig.6 (a). With the increasing specific surface, the performance of VRFB is improved at different temperatures and porosity, but the enhancement of performance becomes gradually smaller. Under relatively sufficient inlet flow rate 30 ml min^{-1} and 1 mm thick electrode, even with the same specific surface area, the VRFB with low porosity electrode achieves higher current density at 0.8 V. The difference is also observed in Fig.6 (b). This is because, with the decreased porosity, the ohmic polarization decreases, which indicates that the increased electronic conductivity is larger than the decreased ionic conductivity. In addition, as mentioned above, the reaction rate constant and the electrolyte ion conductivity both increase with the increase of temperature, decreasing both the activation and ohmic overpotentials. Therefore, VRFB at a higher temperature can achieve larger current density at same operating and electrode structure

parameters. If VRFB switches to thinner electrode, as shown in Fig.6 (c), the performance of VRFB is improved at different temperatures and porosities, as discussed in the previous sub-section. At 0.8 V, specific surface area 2×10^5 m^2 m^{-3} and 1 mm thick electrode, the current density of a VRFB with 0.93 porosity electrode is 1231 mA cm^{-2}, while the current density of VRFB with 0.8 porosity electrode is 1373mA cm^{-2}. In the same condition but 0.5 mm thick electrode, the current density of VRFB with 0.93 porosity electrode is 1639 mA cm^{-2}, while the current density of VRFB with 0.8 porosity electrode is 1798 mA cm^{-2}.

Noteworthy, the inlet flow rate is reduced from 30 ml min^{-1} to 10 ml min^{-1} to further investigate the performance of VRFBs with different porosities after fibre modification. In a large-scale commercial stack, the average flow rate per cm^2 is normally low, which is only around 1 to 2 mL min^{-2} cm^{-2} [43]. In the present model, the battery has a 4 cm^2 active area. When the flow rate is operated at an inlet flow rate of 30 mL min^{-1}, the average flow rate per cm^2 is 7.5 mL min^{-2} cm^{-2}, which can only reflect the battery performance at different temperatures when the flow is relatively sufficient. When the flow rate is operated at an inlet flow rate of 10 mL min^{-1}, the average flow rate per cm^2 is 2.5 mL min^{-2} cm^{-2}, which is closer to the specific flow rate of the stack.

Moreover, from the Fig. 6 (d), when the total flow rate is 10 mL min^{-1}, the polarization curves show obvious concentration losses at all temperatures, and the voltage of the battery decreases rapidly, which can reflect the similar situation in the VRFB stack. The corresponding result analysis can also be used as reference for the VRFB stack. As shown in Fig. 6 (d), it is found that, the VRFB with 0.8 porosity electrode only outperforms the VRFB with 0.93 porosity electrode when the operating voltage > 0.8 V, which is caused by the reduced ohmic loss in electrode with low porosity (Fig.6 (f)). However, when the operating voltage < 0.8 V, the concentration loss becomes dominant, therefore the VRFB with 0.93 porosity electrode performs better.

From Fig.6 (e), the velocity under rib is slightly higher in the 0.8 porosity electrode than that in the 0.93 porosity electrode. The reactant conversion is also higher in the 0.8 porosity electrode at 0.8 V. The surface concentration of reactant is in the range of 17~263 mol m^{-3} in the electrode with 0.8 porosity and is in the range of 33~354 mol m^{-3} in the electrode with 0.93 porosity, as illustrated in Fig.6 (g). With a higher surface concentration, the limiting current density of VRFB with 0.93 porosity electrode is 1439.6 mA cm^{-2} at 0.8V, 323.15 K, while VRFB with 0.8 porosity electrode only reaches 1361 mA cm^{-2}. The high local current density region is wider in 0.93 porosity than 0.8 porosity as shown in Fig.6 (h). From Fig.6 (i), another attractive advantage of using modified high porosity electrodes is the reduction of pressure

drop, especially at low temperature. Due to assembly problems such as sealing and mechanical strength, carbon-based electrodes are not easy to maintain high porosity in VRFB. Therefore, the electrode with modified fibre of 0.9 porosity is a more beneficial choice, achieving better performance at both high and low flow rates and relatively low pressure drop.

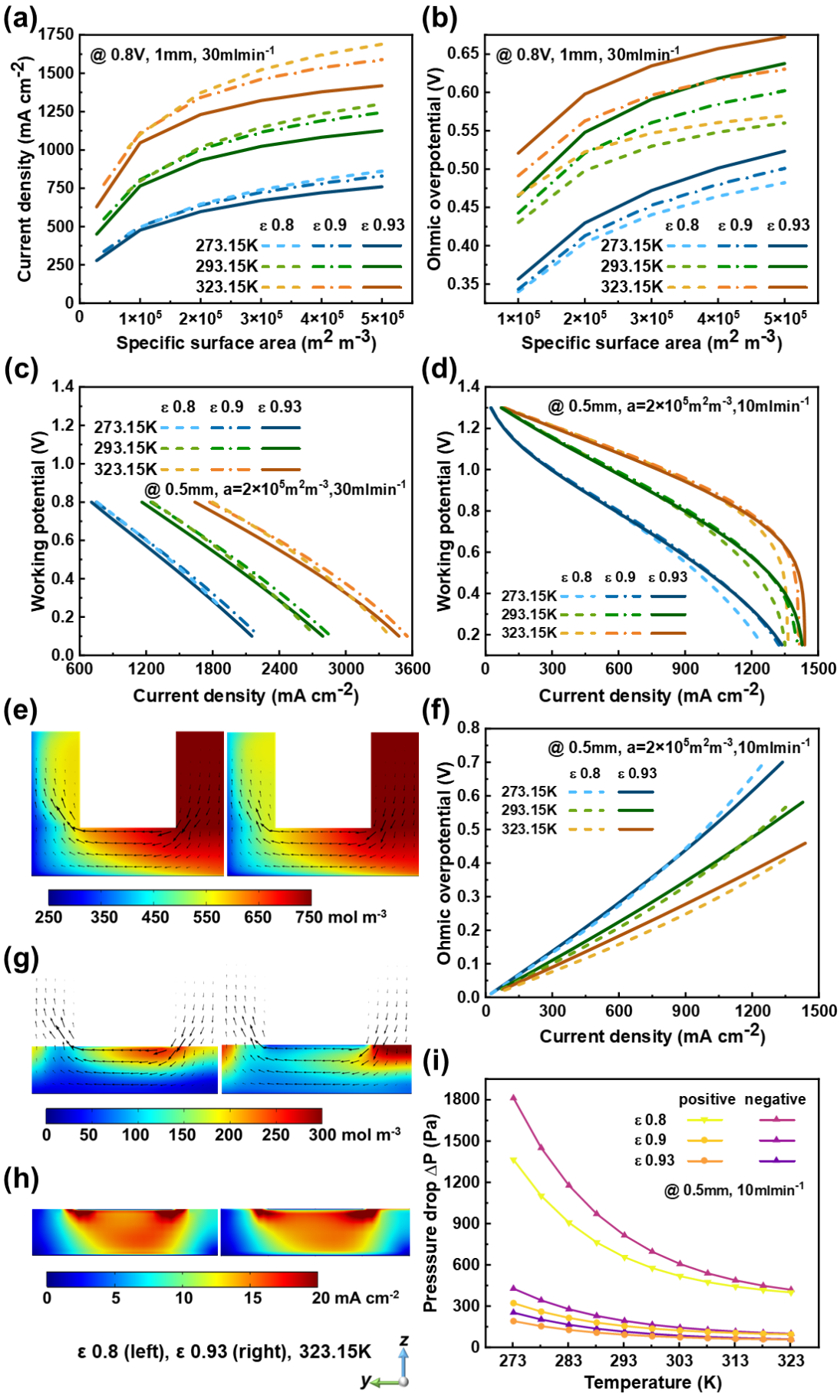
(a)
@ 0.8V, 1mm, 30mlmin-1
Current density (mA cm-2)
Specific surface area (m2 m-3)
ε 0.8 ε 0.9 ε 0.93
273.15K
293.15K
323.15K
(b)
@ 0.8V, 1mm, 30mlmin-1
Ohmic overpotential (V)
Specific surface area (m2 m-3)
(c)
@ 0.5mm, a=2×10^5m^2m^-3,30mlmin-1
Working potential (V)
Current density (mA cm-2)
(d)
@ 0.5mm, a=2×10^5m^2m^-3,10mlmin-1
Working potential (V)
Current density (mA cm-2)
(e)
250 350 450 550 650 750 mol m-3
(f)
@ 0.5mm, a=2×10^5m^2m^-3,10mlmin-1
Ohmic overpotential (V)
Current density (mA cm-2)
(g)
0 50 100 150 200 250 300 mol m-3
(h)
0 5 10 15 20 mA cm-2
ε 0.8 (left), ε 0.93 (right), 323.15K
z
y
(i)
positive negative
@ 0.5mm, 10mlmin-1
Presssure drop ΔP (Pa)
Temperature (K)

485

Fig.6 Effect of specific surface area on current density (a) and ohmic loss (b); Polarization curves of VRFB below 0.8 V (c), below 1.3 V (d); Ohmic loss at 1.3 V (f); V^{5+} bulk concentration distribution (e), V^{5+} surface concentration distribution (g) with velocity component (scale-up factor 50) in yz-direction, and local current density distribution (h) in yz-plane at middle of channel length (x=8 mm); Pressure drop of VRFB with temperature effects (i); All contours at working potential 0.8 V and same conditions as (d).

3.3 Combined effects of the electrode fibre diameter and specific surface area

As mentioned before, the 0.9 porosity is a good choice for electrode with modified fibre. Adjusting electrode fibre diameter is also one of the methods to change electrode permeability. Therefore, the SOC of inlet is set as 0.5 and the electrode porosity is set as 0.9 in this sub-section. Other detailed operating conditions and electrode parameters are labelled in each sub-figure, respectively. The combined effect of electrode fibre diameter and specific surface area at different temperatures on the VRFB performance at 0.8 V are shown in Fig.7 (a). Noteworthy, different fibre diameters in the modified electrodes do not pose a significant impact on the conductivity. However, it can change specific surface area considerably. A thinner electrode with specific surface area of $1\times10^5\ m^2\ m^{-3}$, is chosen for further study, as demonstrated in Fig.7 (b). VRFBs with electrodes using different fibre diameters at 323.15 K show larger performance differences than those at 273.15 K.

Noteworthy, the inlet flow rate is reduced from 30 ml min^{-1} to 10 ml min^{-1} to further investigate the performance of batteries with electrodes using different fibre diameters. Fig.7(c) shows the concentration loss in the electrode with a large fibre diameter is smaller than that in the electrode with a small fibre diameter, as the mass transfer in an electrode with a large fibre diameter can be enhanced considerably. Moreover, at different temperatures, the limiting current density is the same in VRFB with same fibre diameter. From Fig. (d), the modified electrodes with large diameter fibres decrease the pressure drop, especially at low temperature. Referring to Fig.7 (e), the velocity distribution under rib is slightly higher in the electrode with small fibre diameter than that in the electrode with large fibre diameter. The bulk concentration of reactant near outlet channel is slightly lower in the electrode with large fibre diameter at 0.8 V, compared with the electrode with small fibre diameter case. At 273.15 K, 0.8 V, the battery with different fibre diameters electrode achieves almost same current density. This leads to: 1) a small difference in reactant surface concentration distribution with different fibre diameters in Fig.7 (f); 2) a small difference in local current density distribution with different fibre diameters in Fig.7 (g). At 323.15 K, 0.8 V, the battery with larger fibre diameter electrode

519 achieves a higher current density, leading to a lower surface reactant concentration. The local
520 current density distribution in a modified electrode with a larger fibre diameter is more uniform.
521 In addition, the VRFB with the modified electrodes with large diameter fibres shows low
522 pressure drop, especially at a low temperature.
523 It is worth noting that in this section, due to the adaption of the Bruggeman's correlation to
524 calculate the effective conductivity in Eq. (23), which may lead to error without considering
525 the correlation of adapted inter fibre contact areas and fibre diameters. However, because the
526 electrode conductivity is relatively high, the ohmic loss is small compared with the electrolyte.
527 Therefore, neglecting the dependence of ohmic loss on the fibre diameter does not significantly
528 influence the battery performance.

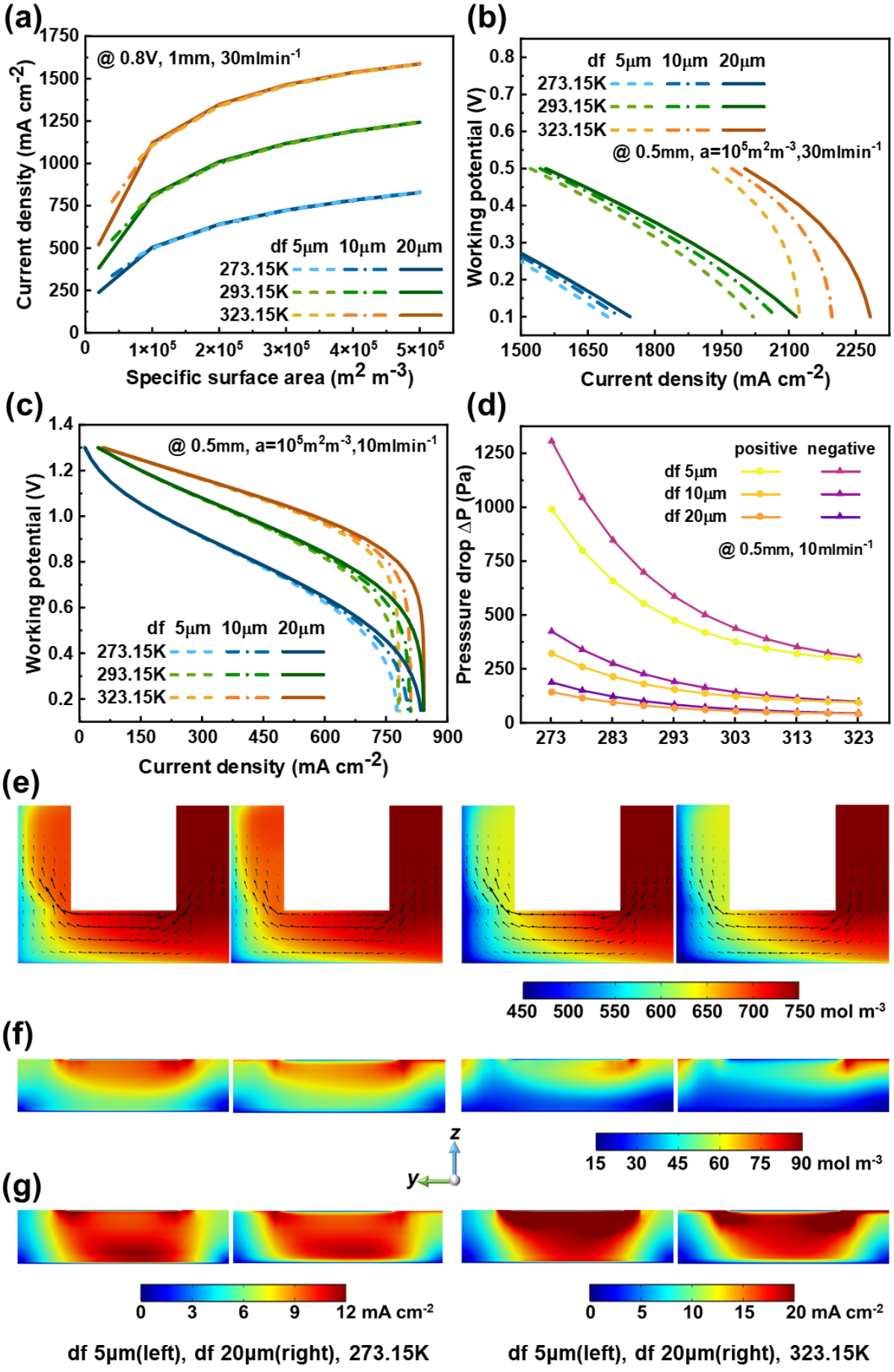
(a)
@ 0.8V, 1mm, 30mlmin-1
Current density (mA cm-2)
Specific surface area (m2 m-3)
df 5μm 10μm 20μm
273.15K
293.15K
323.15K
(b)
df 5μm 10μm 20μm
273.15K
293.15K
323.15K
@ 0.5mm, a=10^5m^2m^-3,30mlmin-1
Working potential (V)
Current density (mA cm-2)
(c)
@ 0.5mm, a=10^5m^2m^-3,10mlmin-1
Working potential (V)
Current density (mA cm-2)
df 5μm 10μm 20μm
273.15K
293.15K
323.15K
(d)
positive negative
df 5μm
df 10μm
df 20μm
@ 0.5mm, 10mlmin-1
Presssure drop ΔP (Pa)
(e)
450 500 550 600 650 700 750 mol m-3
(f)
15 30 45 60 75 90 mol m-3
z
y
(g)
0 3 6 9 12 mA cm-2
0 5 10 15 20 mA cm-2
df 5μm(left), df 20μm(right), 273.15K
df 5μm(left), df 20μm(right), 323.15K

529

Fig.7 Effect of specific surface area on current density (a); Polarization curves of VRFB below 0.5 V (b), below 1.3 V (c); Pressure drop of VRFB with temperature effects (d); V^{5+} bulk concentration distribution (e) with velocity component (scale-up factor 50) in yz-direction, V^{5+} surface concentration distribution (f) and local current density distribution (g) in yz-plane at middle of channel length (x=8 mm); All contours at working potential 0.8 V and same conditions as (c).

3.4 Aligned electrode design with interdigitated flow field

In the previous section, electrodes are simply treated as isotropic. To study the effects of the aligned electrode design at various temperatures, the permeability of electrode is set to be anisotropic. Detailed setting can be found in Eq.(9)-(12) and Fig.3. Unmodified electrode is selected in this sub-section to study the effects of aligned electrode design on the performance of VRFB. The inlet flow rate is 30 ml min^{-1}, SOC of inlet is set as 0.5, the electrode porosity is 0.9 and the carbon electrode fibre diameter is set as 10 μm in this sub-section. Other detailed operating conditions and electrode parameters are labelled in each sub-figure, respectively. By changing the orientation between aligned fibres and flow channel, the influences of xy-plane permeability on the reactant distribution and battery performance are investigated. The effects of different aligned electrode design on the polarization curves at various temperatures are shown in Fig.8 (a-c). It is worth noting that the arrangement angle θ can be controlled by rotating the aligned electrode during installation in practice. Excess parts can be trimmed for other purposes.

At different temperatures, when the current density is less than 200 mA cm^{-2}, the effects of different aligned electrode designs on the activation overpotential are insignificant. With the increasing current density, the electrode with aligned fibre in θ=7° arrangement outperforms other electrode designs. Furthermore, the electrode with aligned fibre in θ=7° arrangement considerably reduces the concentration overpotential, indicating an enhanced mass transfer. VRFB with vertical aligned fibre electrode performs even worse than the VRFB with xy-plane isotropic electrode. VRFB with parallel aligned fibre electrode performs same as the battery with isotropic electrode. The electrode with aligned fibre in θ=45° arrangement also enhances the battery performance but less than θ=7° arrangement.

However, it is still necessary evaluate the influences of different aligned electrode designs on the pressure drop. As shown in Fig.8 (d), all pressure drops and their variations at low temperature are larger than those at high temperature. Even though the θ=7° aligned fibre electrode improves the battery performance the most, it also produces a very large pressure

drop. The vertical aligned fibre electrode has the worst performance and the smallest pressure drop. The parallel aligned fibre electrode has the largest pressure drop without improving the performance of VRFB. Surprisingly, the battery with θ=45° aligned fibre electrode not only improves battery performance significantly, but also reduces the pressure drop. At 323.15 K, the VRFB with θ=45° aligned fibre electrode achieves a limiting current density of 1142 mA cm^{-2}, which is 21% higher than VRFB with xy-plane isotropic electrode. At different temperatures, the pressure drop of the VRFB with θ=45° aligned fibre electrode is at least 36% lower than the pressure drop of VRFB with isotropic electrode.

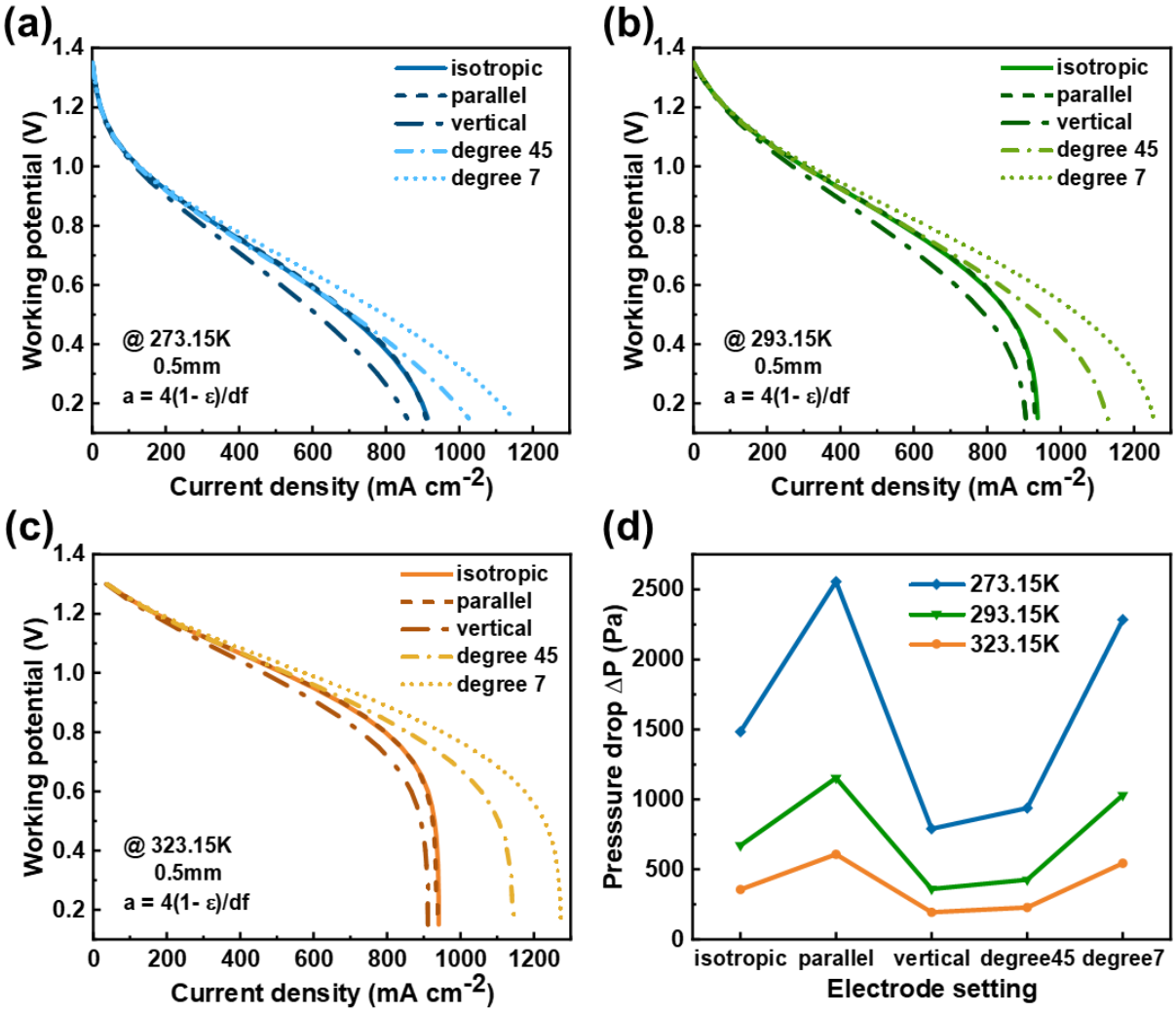

Fig.8 Polarization curves of VRFB with different aligned electrode design at 273.15 K (a), 293.15 K (b) and 323.15 K (c); Pressure drop in negative electrode of different electrode cases (d).

From Fig.9, compared 273.15 K profile with the 323.15 K profile, the velocity distributions of different electrode designs are almost the same. The current density becomes larger, and its distribution becomes less uniform at 323.15 K (noting that the legend scales are different

between two temperature profiles). In xy-plane isotropic, parallel, and vertical electrode, the velocity component directions are similar. Specifically, under the rib, the velocity component direction is oriented perpendicular to the channel (x direction), while under the channel, it is slightly inclined to the outlet direction. In θ=45° and θ=7° aligned fibre electrodes, the direction of velocity component is more consistent with the fibre orientation, especially in the middle section of the battery. The vertical aligned fibre electrode shows the most non-uniform current density distribution.

From Fig.10, compared with 323.15 K case, the local current density is more uniform at 273.15 K. The velocity components of vertical and θ=45° aligned fibre electrodes are extremely high in the region under the rib, while are very low in the region near the membrane. However, the velocity components of isotropic, parallel and θ=7° aligned fibre electrodes are more uniform. Due to small velocity near the membrane, vertical aligned fibre electrode has a low surface concentration of reactant, especially at a high temperature. At 273.15 K, the local current density concentrates near membrane in isotropic, parallel and θ=7° aligned fibre electrodes, while concentrates in the region under the rib in vertical aligned fibre electrode. At 323.15 K, the local current density concentrates in the region under the rib except θ=7° aligned fibre electrode case. Noteworthy, the θ=7° aligned fibre electrode exhibits the most uniform local current distribution.

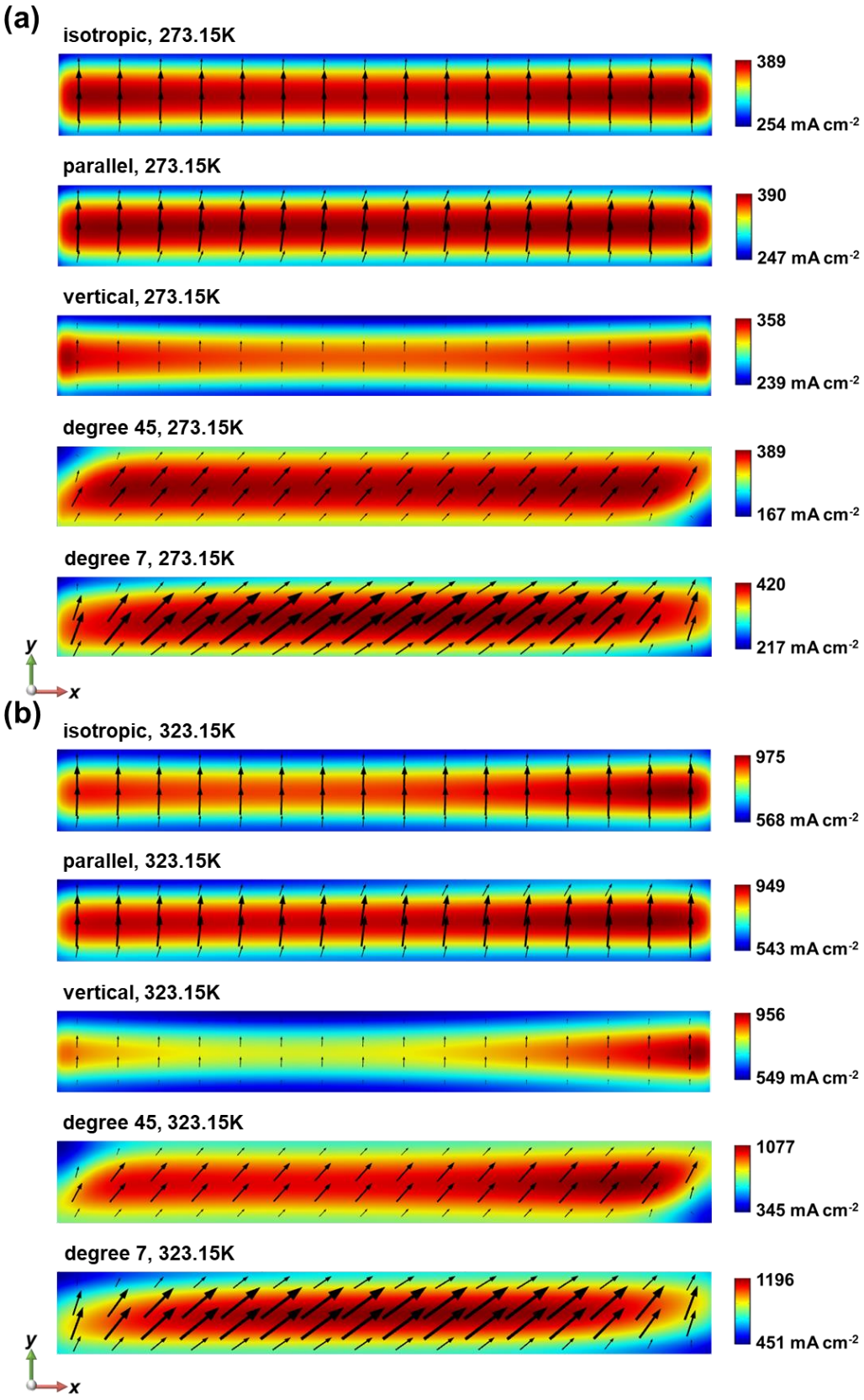

Fig.9 Current density distribution at the middle cross section of membrane in xy-plane with velocity component (scale-up factor 150) in xy-direction at 0.05 mm from the membrane xy-plane of positive electrode at 273.15 K (a) and 323.15 K (b) at working potential 0.8 V.

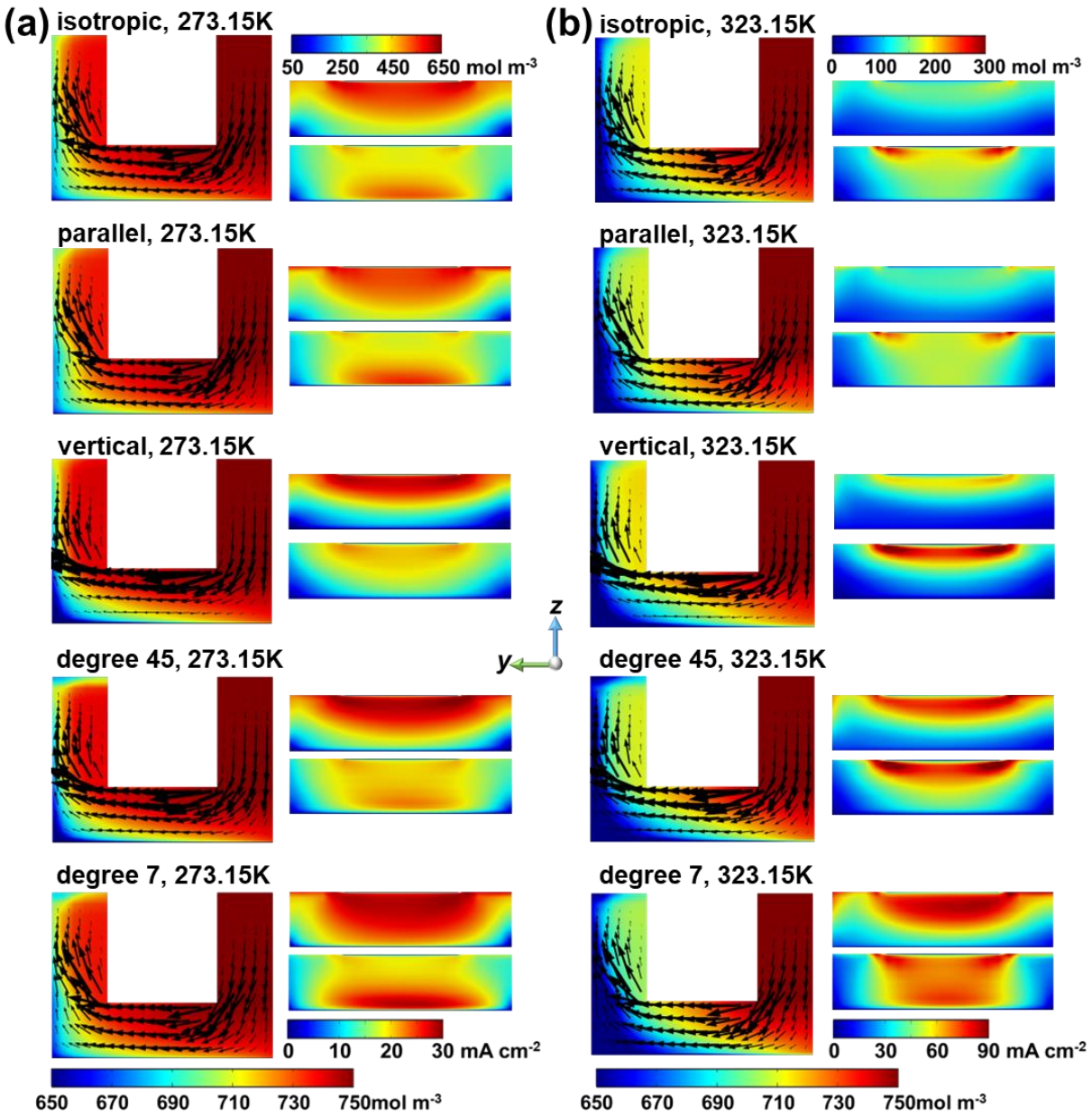

Fig.10 V^{5+} bulk concentration distribution (left in each sub-figure with colour legend at left-bottom) with velocity component (scale-up factor 50) in yz-direction, V^{5+} surface concentration distribution (right-up in each sub-figure with colour legend at right-top) and local current density distribution (right-down in each sub-figure with colour legend at right-down) on yz-plane at middle of channel length (x=8mm) at 273.15 K (a) and 323.15 K (b) at working potential 0.8 V.

3.5 Combined effects of aligned electrode design and specific surface area

The fibre modification can be used in aligned electrodes to further improve the battery performance in this sub-section. The inlet flow rate is 30 ml min^{-1}, SOC of inlet is set as 0.5, the electrode porosity is 0.9 and the carbon electrode fibre diameter is set as 10 μm in this sub-

section. Other detailed operating conditions and electrode parameters are labelled in each sub-figure, respectively. The combined effect of different aligned electrode designs and specific surface area at various temperatures on the VRFB performance are shown in Fig.11. After fibre modification, only θ=7° aligned fibre electrode can further improve battery performance at different temperatures. The θ=45° aligned fibre electrode is only able to increase battery performance with specific surface area 1×10^5 m^2 m^{-3} at 323.15 K. The changes of permeability in xy-plane induced by different aligned electrode designs only have enormous effects on concentration polarization. In electrodes with large specific surface area, the positive impact of the aligned electrode design on battery performance becomes smaller than in the case of low specific surface area electrodes. Under this condition, activation and ohmic overpotentials are the main factors limiting the battery performance.

In general, the practical application of aligned electrode requires full and comprehensive consideration of the battery operating conditions and flow pattern. The fabrication of aligned electrode by electrospinning technology has been successfully applied in the laboratory level batteries since minimal sophisticated equipment or tooling is required by this technique [44]. Electrospinning can easily produce continuous fibres with diameters ranging from tens of nanometres to several microns and several methods for aligning the nanofibers were developed [45]. According to the published experimental data [12], compared with the conventional electrode, the aligned electrode achieves better battery performance and is potentially stable over long battery cycles. Therefore, the design of different orientation of aligned electrode has a certain practical basis. Although the simulation results show that the aligned electrode has advantage under certain conditions, different aligned electrode designs can greatly affect the battery performance, especially the pump consumption, which has potential reference value in the engineering design of large-scale VRFB. In the future, multi-parameter optimization can be performed at the system level to further balance the effects of aligning electrodes and other parameters on battery performance and pump consumption.

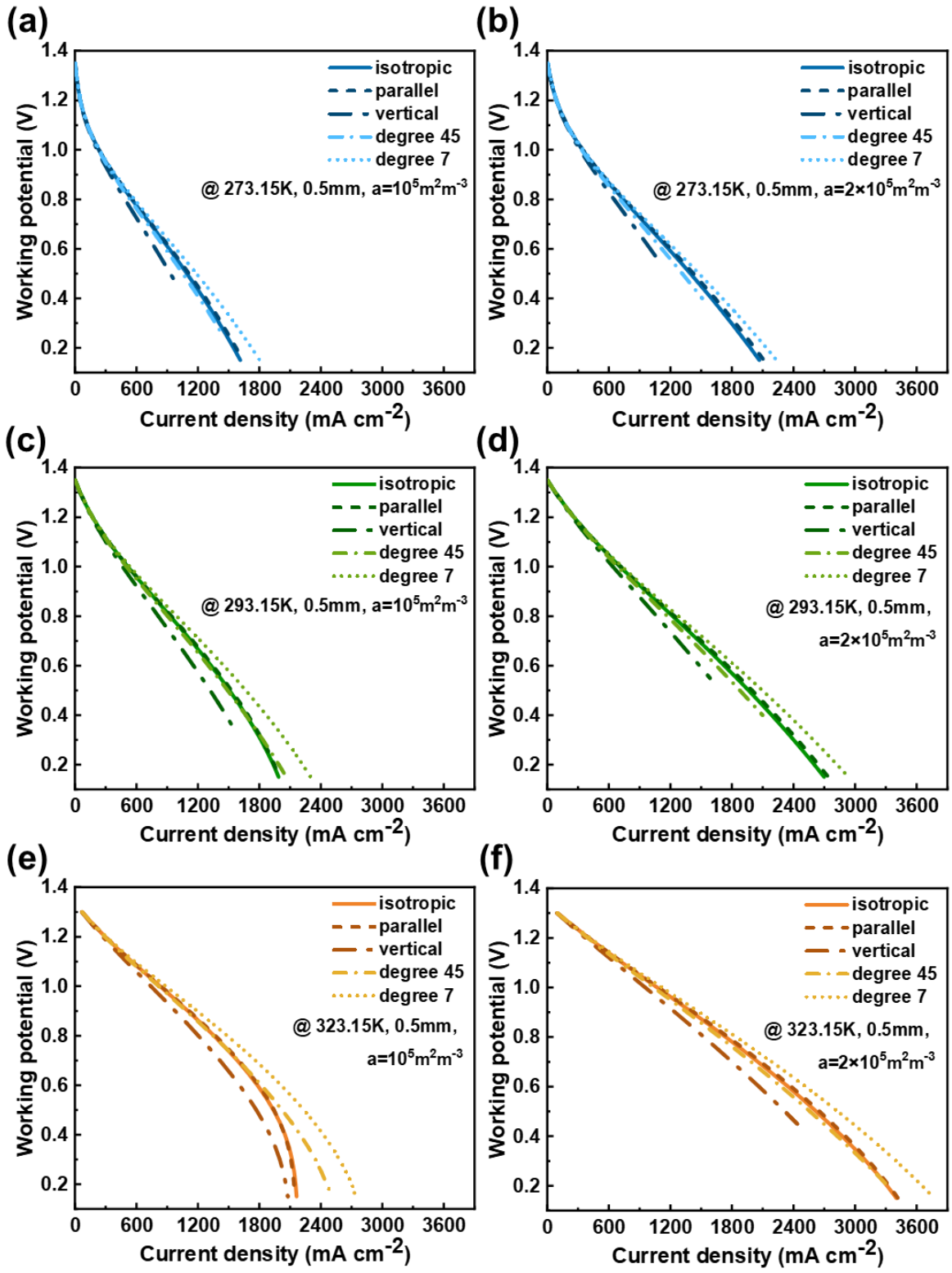

Fig.11 Polarization curves of VRFB with high specific surface area 1×10^5 m^2 m^{-3} at 273.15 K (a), 293.15 K (c) and 323.15 K (e) and higher specific surface area 2×10^5 m^2 m^{-3} at 273.15 K (b), 293.15 K (d) and 323.15 K (f) of different aligned electrode design.

4. Conclusion

In this work, in order to elucidate the combined effects of electrode structural parameters and surface properties the VRFB performance, a 3D model is developed for a VRFB with interdigitated flow field. The fluid flow, species transport, charge transport, and electrochemical reactions behaviour at different temperature are fully considered. The model shows a good agreement with the experimental data from literature. The effects of different aligned electrode designs on battery performance are also discussed in detail.

After fibre modification, 0.5 mm thick electrode has 3 advantages: 1) sufficient total reaction sites reduce activation loss, 2) lower ohmic loss due to thin electrode, 3) lower concentration loss due to enhanced mass transfer. The electrode with modified fibre of 0.9 porosity is a beneficial choice, showing good performance under different inlet flow rates and relatively lower pressure drop. With the increasing fibre diameter in the electrode, although the battery performance can be increased, the pressure drop also increases. Without fibre modification, the VRFB with θ=7° aligned fibre electrode reaches limiting current density of 1270 mA cm^{-2} at 323.15 K, which is 35% higher than VRFB with xy-plane isotropic electrode. However, the θ=7° aligned fibre electrode also produces a very large pressure drop. Remarkably, at 323.15 K, the VRFB with θ=45° aligned fibre electrode achieves limiting current density of 1142 mA cm^{-2}, which is 21% higher than VRFB with xy-plane isotropic electrode. The pressure drop of θ=45° case is 228 Pa, which is 36% lower than that in the VRFB with isotropic electrode. After fibre modification, the positive effects of aligned electrode design on battery performance becomes insignificant, if the specific surface area in the electrode becomes sufficient for electrochemical reactions.

Overall, this model can provide insights into the combined effects of electrode structures and surface properties on VRFB performance and pressure drop at various temperatures. This model also offers a detailed and comprehensive understanding of the complex interaction between the electrode structural parameters and surface properties.

Acknowledgments

This research is supported by a grant under the Theme-based Scheme (project number: T23–601/17-R) from Research Grant Council, University Grants Committee, Hong Kong SAR.

References

[1] Yu J, He Q, Yang G, Zhou W, Shao Z, Ni M. Recent Advances and Prospective in Ruthenium-Based Materials for Electrochemical Water Splitting. ACS Catal 2019;9:9973–10011. https://doi.org/10.1021/acscatal.9b02457.

[2] Li Z, Zhang H, Xu H, Xuan J. Advancing the multiscale understanding on solid oxide electrolysis cells via modelling approaches: A review. Renewable and Sustainable Energy Reviews 2021;141. https://doi.org/10.1016/j.rser.2021.110863.

[3] Li Z, He Q, Wang C, Xu Q, Guo M, Bello IT, et al. Ethylene and power cogeneration from proton ceramic fuel cells (PCFC): A thermo-electrochemical modelling study. J Power Sources 2022;536. https://doi.org/10.1016/j.jpowsour.2022.231503.

[4] Zhao D, Xia Z, Guo M, He Q, Xu Q, Li X, et al. Dynamic hierarchical modeling and control strategy of high temperature proton exchange electrolyzer cell system. Int J Hydrogen Energy 2022;47:22302–15. https://doi.org/10.1016/j.ijhydene.2022.05.067.

[5] Chen Z, Yu W, Liu Y, Zeng Y, He Q, Tan P, et al. Mathematical modeling and numerical analysis of alkaline zinc-iron flow batteries for energy storage applications. Chemical Engineering Journal 2021;405. https://doi.org/10.1016/j.cej.2020.126684.

[6] He Q, Yu J, Guo Z, Sun J, Zhao S, Zhao T, et al. Modeling of Vanadium Redox Flow Battery and Electrode Optimization with Different Flow Fields. E-Prime 2021:100001. https://doi.org/10.1016/j.prime.2021.100001.

[7] Park M, Jung YJ, Kim J, Lee H il, Cho J. Synergistic effect of carbon nanofiber/nanotube composite catalyst on carbon felt electrode for high-performance all-vanadium redox flow battery. Nano Lett 2013;13:4833–9. https://doi.org/10.1021/nl402566s.

[8] Kim Y, Choi YY, Yun N, Yang M, Jeon Y, Kim KJ, et al. Activity gradient carbon felt electrodes for vanadium redox flow batteries. J Power Sources 2018:128–35. https://doi.org/10.1016/j.jpowsour.2018.09.066.

[9] Hu G, Jing M, Wang DW, Sun Z, Xu C, Ren W, et al. A gradient bi-functional graphene-based modified electrode for vanadium redox flow batteries. Energy Storage Mater 2018;13:66–71. https://doi.org/10.1016/j.ensm.2017.12.026.

[10] Wang R, Li Y, He YL. Achieving gradient-pore-oriented graphite felt for vanadium redox flow batteries: Meeting improved electrochemical activity and enhanced mass transport from nano- to micro-scale. J Mater Chem A Mater 2019;7:10962–70. https://doi.org/10.1039/c9ta00807a.

[11] Zhang Z, Bai B, Zeng L, Wei L, Zhao T. Aligned Electrospun Carbon Nanofibers as Electrodes for Vanadium Redox Flow Batteries. Energy Technology 2019;7. https://doi.org/10.1002/ente.201900488.
[12] Sun J, Jiang HR, Zhang BW, Chao CYH, Zhao TS. Towards uniform distributions of reactants via the aligned electrode design for vanadium redox flow batteries. Appl Energy 2020;259. https://doi.org/10.1016/j.apenergy.2019.114198.
[13] Wan S, Liang X, Jiang H, Sun J, Djilali N, Zhao T. A coupled machine learning and genetic algorithm approach to the design of porous electrodes for redox flow batteries. Appl Energy 2021;298. https://doi.org/10.1016/j.apenergy.2021.117177.
[14] Abbas A, Eng XE, Ee N, Saleem F, Wu D, Chen W, et al. Development of reduced graphene oxide from biowaste as an electrode material for vanadium redox flow battery. J Energy Storage 2021;41:102848. https://doi.org/10.1016/j.est.2021.102848.
[15] Abbas A, Abbas S, Bhattarai A, Latiff NM, Wai N, Phan AN, et al. Effect of electrode porosity on the charge transfer in vanadium redox flow battery. J Power Sources 2021;488:229411. https://doi.org/10.1016/j.jpowsour.2020.229411.
[16] Martin J, Schafner K, Turek T. Preparation of Electrolyte for Vanadium Redox-Flow Batteries Based on Vanadium Pentoxide. Energy Technology 2020;8. https://doi.org/10.1002/ente.202000522.
[17] Xiao S, Yu L, Wu L, Liu L, Qiu X, Xi J. Broad temperature adaptability of vanadium redox flow battery - Part 1: Electrolyte research. Electrochim Acta 2016;187:525–34. https://doi.org/10.1016/j.electacta.2015.11.062.
[18] Ressel S, Bill F, Holtz L, Janshen N, Chica A, Flower T, et al. State of charge monitoring of vanadium redox flow batteries using half cell potentials and electrolyte density. J Power Sources 2018;378:776–83. https://doi.org/10.1016/j.jpowsour.2018.01.006.
[19] Yin S, Zhou L, Du X, Yang Y. Influence of temperature on performance of all vanadium redox flow battery: analysis of ionic mass transfer. Ionics (Kiel) 2019;25:593–606. https://doi.org/10.1007/s11581-018-2626-z.
[20] Carta R, Palmas S, Polcaro AM, Tola G. Behaviour of a carbon felt flow by electrodes Part I: Mass transfer characteristics. vol. 21. 1991.
[21] Zhu S, Pelton RH, Collver K. MECHANISTIC MODELLING OF FLUID PERMEATION THROUGH COMPRESSIBLE FIBER BEDS. vol. 50. 1995.
[22] Miscevic M, Santini SR. Fluid Flow Through Randomly Packed Monodisperse Fibers: The Kozeny-Carman Parameter Analysis. 1997.

737 [23] Gostick JT, Fowler MW, Pritzker MD, Ioannidis MA, Behra LM. In-plane and through-
738 plane gas permeability of carbon fiber electrode backing layers. J Power Sources
739 2006;162:228–38. https://doi.org/10.1016/j.jpowsour.2006.06.096.
740 [24] Chan AW, Larive DE, Morgan RJ. Anisotropic Permeability of Fiber Preforms:
741 Constant Flow Rate Measurement. 1993.
742 [25] Banerjee R, Bevilacqua N, Mohseninia A, Wiedemann B, Wilhelm F, Scholta J, et al.
743 Carbon felt electrodes for redox flow battery: Impact of compression on transport properties.
744 J Energy Storage 2019;26:100997. https://doi.org/10.1016/j.est.2019.100997.
745 [26] Newman J, Thomas-Alyea KE. Electrochemical systems. John Wiley & Sons; 2012.
746 [27] Shah AA, Watt-Smith MJ, Walsh FC. A dynamic performance model for redox-flow
747 batteries involving soluble species. Electrochim Acta 2008;53:8087–100.
748 https://doi.org/10.1016/j.electacta.2008.05.067.
749 [28] Corcuera S, Skyllas-Kazacos M. State-of-charge monitoring and electrolyte rebalancing
750 methods for the vanadium redox flow battery. European Chemical Bulletin 2012;1:511–9.
751 [29] Zheng Q, Zhang H, Xing F, Ma X, Li X, Ning G. A three-dimensional model for thermal
752 analysis in a vanadium flow battery. Appl Energy 2014;113:1675–85.
753 https://doi.org/10.1016/j.apenergy.2013.09.021.
754 [30] Oh K, Yoo H, Ko J, Won S, Ju H. Three-dimensional, transient, nonisothermal model of
755 all-vanadium redox flow batteries. Energy 2015;81:3–14.
756 https://doi.org/10.1016/j.energy.2014.05.020.
757 [31] AllenJ. Bard, Parsons R, Jordan J. Standard potentials in aqueous solution. CRC Press;
758 1985.
759 [32] Vatistas N, Marconi PF, Bartolozzi M. Mass-transfer study of the carbon felt electrode.
760 Electrochim Acta 1991;36:339–43. https://doi.org/10.1016/0013-4686(91)85259-A.
761 [33] You X, Ye Q, Cheng P. The Dependence of Mass Transfer Coefficient on the Electrolyte
762 Velocity in Carbon Felt Electrodes: Determination and Validation. J Electrochem Soc
763 2017;164:E3386–94. https://doi.org/10.1149/2.0401711jes.
764 [34] Kok MDR, Jervis R, Tranter TG, Sadeghi MA, Brett DJL, Shearing PR, et al. Mass
765 transfer in fibrous media with varying anisotropy for flow battery electrodes: Direct numerical
766 simulations with 3D X-ray computed tomography. Chem Eng Sci 2019;196:104–15.
767 https://doi.org/10.1016/j.ces.2018.10.049.
768 [35] Kim J, Park H. Electrokinetic parameters of a vanadium redox flow battery with varying
769 temperature and electrolyte flow rate. Renew Energy 2019;138:284–91.

[36] Kroner I, Becker M, Turek T. Determination of Rate Constants and Reaction Orders of Vanadium-Ion Kinetics on Carbon Fiber Electrodes. ChemElectroChem 2020;7:4314–25. https://doi.org/10.1002/celc.202001033.
[37] Nitta I, Hottinen T, Himanen O, Mikkola M. Inhomogeneous compression of PEMFC gas diffusion layer. Part I. Experimental. J Power Sources 2007;171:26–36. https://doi.org/10.1016/j.jpowsour.2006.11.018.
[38] DeBonis D, Mayer M, Omosebi A, Besser RS. Analysis of mechanism of Nafion® conductivity change due to hot pressing treatment. Renew Energy 2016;89:200–6. https://doi.org/10.1016/j.renene.2015.11.081.
[39] Yamamura T, Watanabe N, Yano T, Shiokawa Y. Electron-transfer kinetics of Np3+/ Np4+, NpO2+/ NpO2 2+, V2+/ V3+, and VO2+/ VO2+ at carbon electrodes. J Electrochem Soc 2005;152:A830.
[40] Sum E, Skyllas-Kazacos M. A STUDY OF THE V(II)/V(III) REDOX COUPLE FOR REDOX FLOW CELL APPLICATIONS. vol. 15. 1985.
[41] Skyllas-Kazacos M, Rychick M, Robins R. All-vanadium redox battery. US Patent 4,786,567, 1988.
[42] Bromberger K, Kaunert J, Smolinka T. A Model for All-Vanadium Redox Flow Batteries: Introducing Electrode-Compression Effects on Voltage Losses and Hydraulics. Energy Technology 2014;2:64–76. https://doi.org/10.1002/ente.201300114.
[43] Wei L, Guo ZX, Sun J, Fan XZ, Wu MC, Xu JB, et al. A convection-enhanced flow field for aqueous redox flow batteries. Int J Heat Mass Transf 2021;179. https://doi.org/10.1016/j.ijheatmasstransfer.2021.121747.
[44] Liu S, Kok M, Kim Y, Barton JL, Brushett FR, Gostick J. Evaluation of Electrospun Fibrous Mats Targeted for Use as Flow Battery Electrodes. J Electrochem Soc 2017;164:A2038–48. https://doi.org/10.1149/2.1301709jes.
[45] Xue J, Wu T, Dai Y, Xia Y. Electrospinning and electrospun nanofibers: Methods, materials, and applications. Chem Rev 2019;119:5298–415. https://doi.org/10.1021/acs.chemrev.8b00593.